Detailed Spectroscopic Analysis of Half-Met Hemocyanins: Mixed-Valent Contributions to Electronic Properties and Structure

T. David Westmoreland, Dean E. Wilcox, Michael J. Baldwin, William B. Mims,[†] **and Edward I. Solomon***

Contribution from the Department of Chemistry, Stanford University, Stanford, California 94305. Received October 31, 1988

Abstract: The half-met-L derivatives of hemocyanin have a mixed-valent [Cu(II)Cu(I)] site and have played an important role in understanding coupled binuclear copper sites because of their unique chemical and spectroscopic features. Competitive ligand binding experiments are presented which demonstrate that exogenous ligands, L, bind to the site with unusually high equilibrium binding constants. For L = N_3^-, the temperature dependencies of the binding constants to half-met, fully oxidized met, and fully reduced deoxy derivatives provide insight into the thermodynamic origin of this high-affinity chemistry. For the series L = NO_2^-, Cl^-, Br^-, and I^-, low-temperature optical absorption, circular dichroism, and low-temperature magnetic circular dichroism spectra are presented. Variable-frequency EPR spectra have been obtained and simulated and the linear electric field effect (LEFE) on the *g* values has been measured using electron spin–echo spectroscopy. From the excited-state spectroscopy the ligand field transitions of the Cu(II) in the site have been assigned, and this copper has been determined to have a tetragonal geometry. The intervalent transfer transition (corresponding to a Cu(I) → Cu(II) charge-transfer transition in the dimer) has been definitively assigned and its energy has been used in a ligand field calculation to determine the effective geometry of the Cu(I) as distorted tetrahedral. Analysis of the IT band has also provided an estimate of delocalization in the ground state. Copper hyperfine coupling constants from the EPR simulations have allowed an independent estimate of delocalization which has been compared to the optically determined value. Both results correlate with a superexchange pathway through the exogenous ligand and demonstrate that L bridges the two coppers in the half-met site. Additionally, delocalization has been determined to lead to a large noncoincidence of the principal axes of the dimer *g* tensor and the copper hyperfine tensors. LEFE measurements have proved to be an important probe of mixed-valent systems, and the effects of delocalization on the magnitude of the LEFE shifts have been determined. From these studies a spectroscopically effective half-met-L site has been determined for hemocyanin and tyrosinase which is significantly different from that of the type 3 site in laccase. These differences appear to correlate with the reactivity of these coupled binuclear active sites.

The hemocyanins function as oxygen transport proteins for molluscs and arthropods.[1,2] The oxygen binding site contains two copper(II) ions in the oxygenated protein. Through a variety of chemical and spectroscopic studies, a spectroscopically effective model for the active site of oxyhemocyanin has been developed[1] which is summarized in Figure 1A. The site consists of two tetragonally coordinated Cu(II) ions with peroxide bridging the metals symmetrically in the equatorial plane. A second endogenous bridge (OR⁻) also appears to be present which plays a major role in antiferromagnetically coupling the Cu(II) ions.[3] The only hemocyanin for which an X-ray crystal structure is currently available is the deoxyhemocyanin of *Panulirus interruptus*.[4] At present resolution (3.2 Å) this deoxy site (Figure 1B) contains two Cu(I) ions, each coordinated by two histidines at ~2.0 Å and a more distant histidine at ~2.6 Å arranged in a trigonal antiprism structure.

The chemically generated half-met-L derivatives[5,6] represent an important intermediate redox state between the fully oxidized oxy site, [Cu(II)Cu(II)], and the fully reduced deoxy site, [Cu(I)Cu(I)]. Depending on the nature of the exogenous ligand, L, these derivatives exhibit unusual spectroscopic features and chemical properties. The sites have magnetic properties characteristic of an $S = {}^1/_2$ system and correspond to a mixed-valent [Cu$_A$(II)Cu$_B$(I)] formulation. A variety of exogenous ligands (L = Cl⁻, Br⁻, I⁻, NO_2^-, OAc⁻, N_3^-, SCN⁻, CN⁻) have been shown to bind to copper in the site. The EPR spectra for L = Br⁻, I⁻, and several other half-met derivatives, show complex hyperfine patterns which are indicative of coupling of the unpaired electron to both copper atoms in the site. Additionally, for a number of the half-met derivatives a low-energy optical absorption band is observed which is not observed in mononuclear copper complexes. This new absorption band has been proposed to be an intervalent transfer transition (vide infra). These chemical and spectroscopic features are particularly significant when compared with other

proteins with similar coupled binuclear copper sites. Tyrosinase, which catalyzes the oxidation of monophenols to *o*-diphenols and *o*-quinones, has also been characterized in a half-met form which exhibits spectroscopic properties similar to those of the half-met hemocyanins.[7] In contrast, the multicopper oxidase, laccase, has been produced in a half-met T2D (Type 2 depleted) form which shows none of the unusual ground- and excited-state spectral properties noted above.[8]

Half-met hemocyanin binds exogenous ligands with unusually high affinities.[6] In contrast, met-apo hemocyanin, in which a Cu(I) has been removed, [Cu(II)—], exhibits ligand binding properties similar to those of aqueous Cu(II) complexes.[6] Additionally, if half-met-L is reacted with CO, L can be easily removed by dialysis. This observation has been interpreted[6] in terms of a model in which L bridges the copper ions but is competitively displaced from the Cu(I) by CO to give a nonbridging derivative in which L is bound

(1) (a) Solomon, E. I. In *Copper Proteins*; Spiro, T. G., Ed.; Wiley-Interscience: New York, 1981; p 41. (b) Eickman, N. C.; Himmelwright, R. S.; Solomon, E. I. *Proc. Natl. Acad. Sci. U.S.A.* **1979,** *76,* 2094.

(2) van Holde, K. E.; Miller, K. I. *Q. Rev. Biophys.* **1982,** *15,* 1.

(3) (a) Solomon, E. I.; Dooley, D. M.; Wang, R. H.; Gray, H. B.; Cerdonio, M.; Mogno, F.; Romani, G. L. *J. Am. Chem. Soc.* **1976,** *98,* 1029. (b) Dooley, D.; Scott, R. A.; Ellinghaus, J.; Solomon, E. I.; Gray, H. B. *Proc. Natl. Acad. Sci. U.S.A.* **1978,** *75,* 3019.

(4) (a) Gaykema, W. P. J.; Hol, W. G. J.; Vereijken, J. M.; Soeter, N. M.; Bak, H. J.; Beintema, J. J. *Nature (London)* **1984,** *309,* 23. (b) Gaykema, W. P. J.; Volbeda, A.; Hol, W. G. J. *J. Mol. Biol.* **1985,** *187,* 255.

(5) (a) Himmelwright, R. S.; Eickman, N. C.; Solomon, E. I. *Biochem. Biophys. Res. Commun.* **1978,** *81,* 237. (b) Himmelwright, R. S.; Eickman, N. C.; Solomon, E. I. *Biochem. Biophys. Res. Commun.* **1978,** *81,* 243. (c) Himmelwright, R. S.; Eickman, N. C.; Solomon, E. I. *Biochem. Biophys. Res. Commun.* **1978,** *84,* 300.

(6) Himmelwright, R. S.; Eickman, N. C.; Solomon, E. I. *J. Am. Chem. Soc.* **1979,** *101,* 1576.

(7) Himmelwright, R. S.; Eickman, N. C.; LuBien, C. D.; Lerch, K.; Solomon, E. I. *J. Am. Chem. Soc.* **1980,** *102,* 7339.

(8) (a) Spira, D. J.; Solomon, E. I. *J. Am. Chem. Soc.* **1987,** *109,* 6421. (b) Spira, D. J.; Solomon, E. I. *Biochem. Biophys. Res. Commun.* **1983,** *112,* 729.

†Consultant: Exxon Research and Engineering Co., Annandale, NJ 08801.
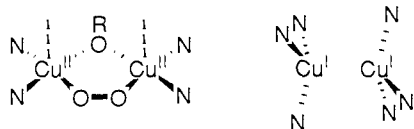
Figure 1. Spectroscopically effective oxyhemocyanin active site[1] (left) and crystallographically defined deoxyhemocyanin active site[4] (right).

with normal affinity. Again, half-met T2D laccase does not exhibit this unusual high-affinity exogenous ligand binding,[8] while half-met tyrosinase does.[7] The origin of high-affinity binding in half-met hemocyanin thus has implications concerning the nature of ligand binding, the electronic consequences of ligand bridging, and thermodynamic stabilization of the half-reduced site.

A theoretical framework for understanding mixed-valent complexes has been developed by Hush,[9] and most treatments of mixed-valent systems are cast in terms of this formalism. The characteristic delocalization parameter for a mixed-valent complex is α^2, which is defined in eq 1 where the ground-state wave function

$$|G\rangle = (1 - \alpha^2)^{1/2}|\psi[Cu_A(II)Cu_B(I)]\rangle + \alpha|\psi[Cu_A(I)Cu_B(II)]\rangle \tag{1}$$

is expressed in terms of the wave functions for two states in which the unpaired electron is localized completely on either Cu_A or Cu_B. Robin and Day[10] have provided a classification scheme for mixed-valent complexes based on the value of α^2. A system in which the unpaired electron is completely localized on Cu_A, $\alpha^2 = 0$, is called a Class I complex, and its properties are the sum of those for the individual oxidized and reduced ions. The completely delocalized case, $\alpha^2 = 0.5$, belongs to Class III. These systems generally exhibit properties different from those of the individual ions. Delocalization in Class II complexes is in the range $0 < \alpha^2 < 0.5$. In general their properties resemble those of the individual ions but are significantly perturbed due to the interaction between the sites. The most commonly observed spectroscopic perturbation is the presence of an intervalent transfer (IT) absorption band which corresponds to optical charge transfer of the unpaired electron from Cu_B to Cu_A giving the IT excited state described by eq 2.

$$|IT\rangle = \alpha|\psi[Cu_A(II)Cu_B(I)]\rangle - (1 - \alpha^2)^{1/2}|\psi[Cu_A(I)Cu_B(II)]\rangle \tag{2}$$

The Hush formalism provides a means of estimating α^2 from the integrated intensity of the IT band. Since the magnitude of hyperfine coupling to an atom is related to the spin density at the nucleus, it is possible to obtain an independent estimate of α^2 based on an EPR determination of the ground-state wave function if hyperfine couplings can be observed. Unlike the previously more extensively investigated ruthenium and iron mixed-valent systems,[11] several of the half-met-L hemocyanins exhibit hyperfine couplings to the two coppers. Thus, the EPR parameters for half-met-L hemocyanin should provide an independent probe of the ground-state wave function.

In this study the thermodynamic parameters of the binding of azide to met-aquo ([Cu(II)Cu(II)]), half-met-aquo ([Cu(II)-Cu(I)]), and deoxy ([Cu(I)Cu(I)]) hemocyanins have been estimated from the temperature dependence of the equilibrium binding constants. These results define the thermodynamic origin of high affinity azide binding at the half-met site and establish relationships between the redox couples involved and the disproportionation constant for half-met hemocyanin. Low-temperature absorption, circular dichroism (CD), and low-temperature magnetic circular dichroism (LT-MCD) data for a series of half-met hemocyanin derivatives are presented. From the selection rules for each technique, the ligand field and intervalent transfer bands have been assigned. The energies of the ligand field bands

have been interpreted in terms of the geometry dependence of the one-electron orbital splittings of Cu(II) which allows an estimate of the effective geometry of $Cu_A(II)$ in the half-met site. The parameters of the IT bands have been used to obtain ground-state delocalization coefficients through a Hush analysis of the intensities. Further, it has been possible to calculate the effective geometry of $Cu_B(I)$ in the site based on a ligand field analysis of the IT band energy. Variable-frequency EPR spectra have been obtained and simulated and from the spin-Hamiltonian parameters an independent measure of delocalization has been obtained and compared to the optical method of determining α^2. Finally, a new spectroscopic probe of the ground-state wave function in this mixed-valent site has been employed: the linear electric field effect (LEFE) on the EPR spectrum as measured by the electron spin–echo method. This effect can only be observed if the unpaired electron has noncentrosymmetric site symmetry. The odd parity component of the ground-state wave function should vary systematically as the electron is increasingly delocalized over the two metal centers. This study has provided considerable insight into the origins of the unusual chemical and spectroscopic features of half-met hemocyanin (and tyrosinase) and the factors which give rise to the dramatic differences in the chemistry and spectroscopy of the half-met coupled binuclear (Type 3) site in laccase.

Experimental Section

Busycon canaliculatum was obtained from Woods Hole Marine Biological Institute. The hemolymph was extracted by foot puncture and was centrifuged to give a dark blue pellet of oxyhemocyanin. The pellet was dissolved in phosphate buffer to give a final concentration of approximately 1 mM (unless otherwise specified all solutions are in 0.1 M aqueous phosphate buffer, pH = 6.3). Half-met hemocyanin was produced[6] by direct addition of approximately 30-fold stoichiometric excess of $NaNO_2$ and ascorbic acid to a 1–2 mM solution of oxyhemocyanin. After 1 to 2 h of gentle stirring at room temperature, the green solution was dialyzed against two changes of fresh phosphate buffer at 4 °C to give the half-met-NO_2^- derivative. The half-met-N_3^- derivative was produced by dialysis of half-met-NO_2^- against 0.2 M NaN_3 for several hours followed by dialysis against two changes of fresh buffer. Half-met-aquo was obtained by dialysis of half-met-N_3^- against 0.2 M NaOAc buffer (pH = 5.0) to produce a half-met-OAc⁻ derivative, followed by dialysis against phosphate buffer (pH = 6.3) for approximately 72 h. Other half-met-L⁻ derivatives (L⁻ = Cl⁻, Br⁻, I⁻) were obtained by dialyzing half-met-N_3^- or half-met-aquo against 0.2 M NaL for 8–10 h, followed by dialysis for several hours against two changes of fresh buffer. Met-aquo hemocyanin[12] was obtained by a modified procedure in which a solution of oxyhemocyanin was dialyzed against several changes of 0.2 M NaF in 0.2 M NaOAc buffer (pH = 5.0) at 35 °C for approximately 72 h. The solution was then dialyzed against several changes of 0.1 M phosphate buffer (pH = 6.3) at 4 °C to give the met-aquo form, in which there is no evidence for bound fluoride. The deoxy hemocyanin sample for the binding constant experiments was obtained by extensive anaerobic dialysis of oxyhemocyanin against buffer with a continuous N_2 purge. The deoxy samples were subsequently manipulated under an Ar atmosphere in the presence of <8 ppm of O_2. Total protein concentrations were determined from the optical absorbance at 280 nm ($\epsilon = 7.7 \times 10^4$ M^{-1} cm^{-1}).[13] For the EPR experiments, the solutions were concentrated to approximately 3 mM with a Millipore immersible ultrafiltration unit. The LT-MCD experiments were carried out with solutions of 0.2 M phosphate (pH = 6.3) in 2:1 (v/v) glycerol–water. This composition was chosen to assure formation of an optically transparent glass at low temperatures. EPR spectra of these solutions showed some sharpening of the signals relative to purely aqueous samples, but no detectable changes in *g* values or hyperfine features.

X- and Q-band EPR spectra were obtained on a Bruker ER-220D instrument and were the computer signal average of 4 (X-band) or 16 (Q-band) scans. S-band spectra were obtained with a Bruker S-band bridge using a split ring resonator cavity and were typically the average of 16 scans. The linear electric field effect (LEFE) measurements were made at 4.2 K with X-band frequencies (9.4–9.7 GHz) using an electron spin–echo instrument described elsewhere.[14] The LEFE was measured by determining the decrease in the spin–echo amplitude upon application of an electric field and is quantified by the shift parameter, *σ*, calculated

(9) (a) Hush, N. S. *Prog. Inorg. Chem.* **1967**, *8*, 391. (b) Hush, N. S. *Electrochim. Acta* **1968**, *13*, 1005.
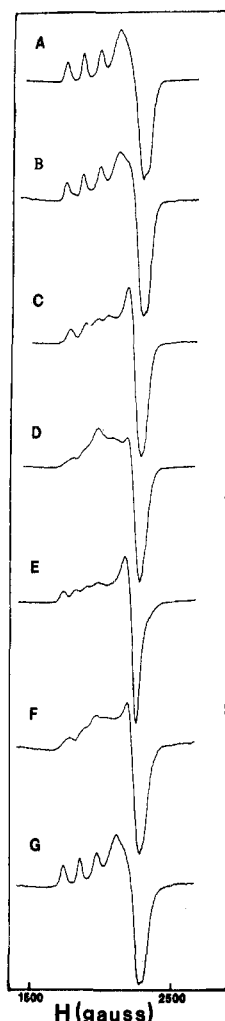(10) Robin, M. B.; Day, P. *Adv. Inorg. Radiochem.* **1967**, *10*, 247.
(11) Creutz, C. *Prog. Inorg. Chem.* **1983**, *30*, 1.

(12) Witters, R.; Lontie, R. *FEBS Lett.* **1975**, *60*, 400.
(13) Nickerson, K. W.; van Holde, K. E. *Comp. Biochem. Physiol.* **1971**, *39B*, 855.
(14) Mims, W. B. *Rev. Sci. Instrum.* **1974**, *45*, 1583.

A

B

C

D

E

F

G

1500   2500
H (gauss)

Figure 2. X-band EPR spectra (100 K) of (A) half-met-NO_2^-; (B) half-met-NO_2^- + 10-fold stoichiometric excess N_3^-; (C) half-met-xs-N_3^-, from dialysis of half-met-NO_2^- against 0.2 M NaN_3; (D) half-met-N_3^-, from dialysis of half-met-xs-N_3^- against buffer; (E) half-met-aquo; (F) half-met-aquo + 10-fold excess N_3^-; (G) half-met-aquo + 10-fold excess NO_2^-.

from the relationship $\sigma = d/6\nu(\tau V)_{1/2}$, where d is the sample thickness, ν is the microwave frequency, and $(\tau V)_{1/2}$ is the product of the time τ between the echo-generating pulses and the voltage V which causes a 50% reduction in the echo amplitude. UV–vis spectra were obtained on either a Cary Model 17 spectrophotometer or, for the equilibrium binding constant determinations, an HP 8450A diode array spectrophotometer. CD spectra were measured with a JASCO J-500C spectropolarimeter. The MCD spectrometer employed an Oxford Instruments SM4 superconducting magnet in the beam path of the CD spectrometer. The details of this instrument have been described elsewhere.[15] The samples were mounted between two quartz disks using an ~3-mm thick rubber gasket as a spacer. Depolarization was checked (<2% in all cases) by comparing the CD spectra of (+)-nickel tartrate in front of and behind the sample and magnet. The spectra given in the Results were obtained at 4.2 K with a 6.0-T field.

Results

(A) Ligand Binding. There are a number of unusual features to the substitution chemistry of the half-met hemocyanin site. The EPR spectrum of half-met-NO_2^- is shown in Figure 2A. Extensive dialysis (>14 days) of this derivative produces no change in the EPR or optical properties. It has been suggested[16] that there

(15) Spira, D. J.; Allendorf, M. D.; Solomon, E. I. *J. Am. Chem. Soc.* **1986**, *108*, 5318.

(16) (a) Tahon, J.-P.; van Hoof, D.; Vinckier, C.; Witters, R.; de Ley, M.; Lontie, R. *Biochem. J.* **1988**, *249*, 891. (b) Salvato, B.; Giacometti, G. M.; Beltramini, M.; Zilio, F.; Giacometti, G.; Magliozzo, R. S.; Peisach, J. *Biochemistry* **1989**, *28*, 680.

is no exogenous ligand (i.e., other than water derived) bound to the site in this form. However, from the chemistry described below, it is clear that this is *not* a half-met-aquo derivative but, in fact, has a NO_2^- related ligand bound with high affinity to the site. This derivative has thus been labeled half-met-NO_2^-. Direct addition of 10-fold stoichiometric excess of NaN_3 to half-met-NO_2^- gives the spectrum in Figure 2B, which is not significantly perturbed from Figure 2A. Dialysis (~4 h) of half-met-NO_2^- against 0.2 M NaN_3 gives the spectrum in Figure 2C. The fact that a large excess of azide is necessary to effect a change in the EPR would seem to imply a relatively small binding constant for azide with half-met hemocyanin. Dialysis of this solution against phosphate buffer gives the spectrum in Figure 2D which is clearly different from Figure 2, A–C. For the derivative in Figure 2D resonance Raman spectroscopy has shown[17] an intraazide stretch at 2040 cm^{-1} indicating that azide is bound to the site and thus the derivative is half-met-N_3^-. Figure 2C has been previously shown[6] to correspond to a form with two azide ions bound at the site, half-met-xs-N_3^-. The second azide can be readily dialyzed away as demonstrated in Figure 2, C and D. However, extensive dialysis of half-met-N_3^- yields no change in the spectrum, indicating a very large binding constant for azide at the half-met site. If no strongly bound exogenous ligand were present in half-met-NO_2^-, the half-met-NO_2^- plus 10-fold N_3^- reaction (Figure 2B) would be expected to proceed to half-met-N_3^- (Figure 2D) which is not the case. These results then require that half-met-NO_2^- contains an exogenous ligand bound with high affinity that is displaced by competitive binding of azide in high concentrations.

These conclusions are further supported by the chemistry of the half-met-aquo derivative which was prepared as described in the Experimental Section and has the EPR spectrum shown in Figure 2E. The label half-met-aquo indicates that no exogenous ligand is bound since the signal is different from that of the half-met-OAc$^-$ precursor and the only potential ligands remaining in the system are derived from water. The rate of conversion of half-met-OAc$^-$ to half-met-aquo increases as the pH of the buffer is raised, suggesting that competitive binding of OH$^-$ may be responsible for the observed chemistry. Direct addition of a 10-fold excess of N_3^- to half-met-aquo yields the spectrum in Figure 2F which shows ~80% conversion to half-met-N_3^-. This is in contrast to the reaction of a 10-fold excess of N_3^- with half-met-NO_2^- which gave no appreciable reaction (Figure 2B). Further, the addition of a 10-fold stoichiometric excess of NO_2^- to half-met-aquo at pH = 6.3 gives the spectrum in Figure 2G which is identical with the original half-met-NO_2^- spectrum. These results demonstrate that the exogenous ligand bound with high affinity in the half-met derivative initially formed from oxyhemocyanin is derived from NO_2^-. The chemistry of half-met hemocyanin can therefore be rationalized in terms of competitive high-affinity binding of exogenous ligands. The general exogenous ligand substitution reactivity pattern described above and earlier results for other ligands[6] are summarized in Scheme I.

In order to determine the origin of this high affinity, the thermodynamic parameters of azide binding to half-met-aquo hemocyanin were estimated by temperature-dependent equilibrium binding constant experiments. Parameters for azide binding to met-aquo and deoxy hemocyanin were also obtained for comparison. While the binding constants, K_{eq}, can be determined relatively accurately, it is important to note that calorimetric techniques are preferred for determining enthalpies of reaction and the data presented here are measured over a rather limited range of temperatures. Thus the enthalpies and entropies presented must be considered useful estimates but only accurate to within about 20%.
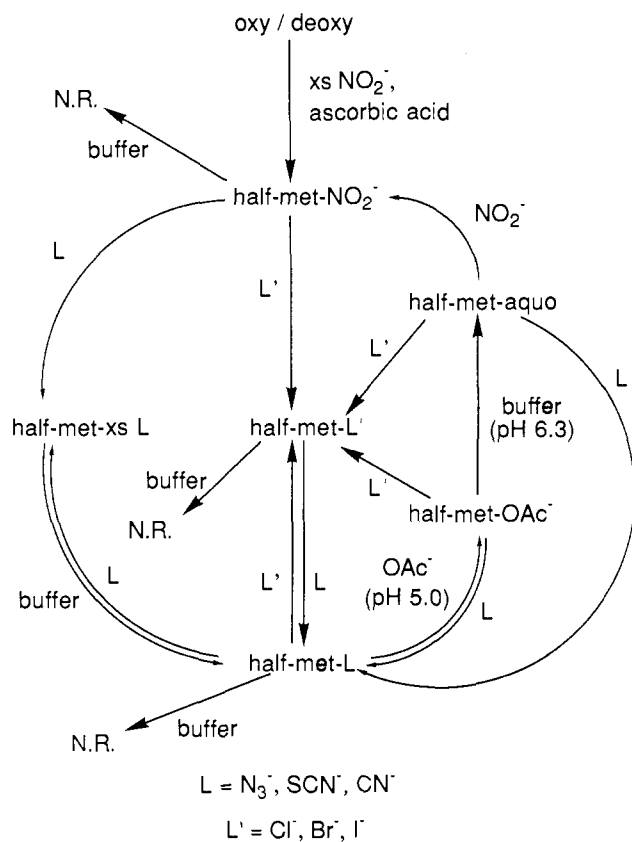
The binding constant for azide to met-aquo was determined by preparing N_2 purged solutions with known concentrations of met-aquo and N_3^-. These solutions were thermostated at each temperature for at least 4 h to ensure that equilibrium had been

(17) Himmelwright, R. S.; Eickman, N. C.; Solomon, E. I. In *International Symposium on Oxidases and Related Redox Systems III*; King, T. E., et al., Eds.; Pergamon Press: New York, 1982; p 263.

Scheme I

$$L = N_3^-, SCN^-, CN^-$$

$$L' = Cl^-, Br^-, I^-$$

Table I. Thermodynamic Parameters for Azide and Thioacetamide Binding to Met, Half-Met, and Deoxy Hemocyanins

	ΔH (kJ/mol)	ΔS (J/mol-K)	ΔG^{298} (kJ/mol)	K_{eq}^{298}
met + N_3^-	-26 ± 6	-50 ± 20	-11 ± 6	100
half-met + N_3^-	$+90 \pm 30$	$+400 \pm 100$	-25 ± 30	2.4×10^4
deoxy + TA	-80 ± 10	-200 ± 50	-20 ± 10	4.0×10^3
deoxy-TA + N_3^-	0 ± 60	-40 ± 200	$+10 \pm 60$	2.0×10^{-2}
deoxy + N_3^-	-80 ± 60^a	-240 ± 200^a	-10 ± 60	80

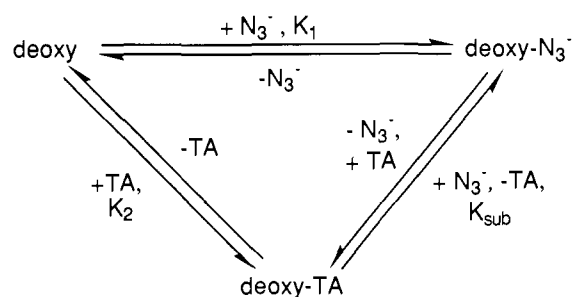^{a} Calculated from the deoxy + TA and deoxy-TA + N_3^- parameters as described in the text.

established. Absorption spectra were measured and the intensity at 455 nm ($\epsilon \sim 900$ M^{-1} cm^{-1}, Cu(II) $\leftarrow N_3^-$ CT)[18] was used to determine the concentration of met-N_3^-. Previous studies[18] have shown that absorbance at this wavelength is associated with the binding of a single azide. Equilibrium binding constants were determined at each temperature from the expression

$$K_{eq} =$$
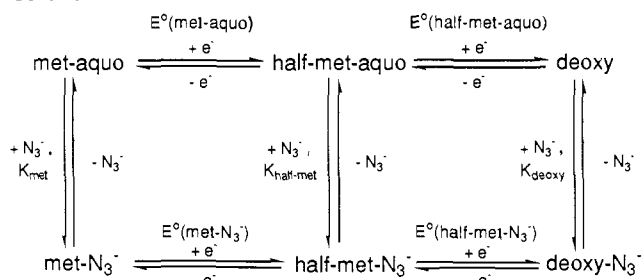$$[\text{met-}N_3^-]/([\text{met-aquo}]_0 - [\text{met-}N_3^-])([N_3^-]_0 - [\text{met-}N_3^-])$$

where [met-aquo]$_0$ and [N_3^-]$_0$ are the total concentrations of met-aquo and azide added to the solution. Figure 3A shows a plot of $R \ln (K_{eq})$ versus $1/T$. Since $R \ln (K_{eq}) = -\Delta H/T + \Delta S$, the enthalpy and entropy of binding can be estimated from the slope and intercept, respectively. The results of a least-squares fit of the data shown in the figure are given in Table I.

Half-met-aquo hemocyanin was prepared as described above. The procedure for the binding constant experiments was the same as that used for the met-aquo experiment. For these experiments, the Cu(II) $\leftarrow N_3^-$ CT transition at 478 nm ($\epsilon = 1000$ M^{-1} cm^{-1})[6] was used to measure the concentration of half-met-N_3^-. Scatchard plots of azide titrations at constant temperature (Figure 3B, inset) confirm that only one ligand is bound per site ($n = 1.1 \pm 0.1$) at the concentrations of azide employed. A fit of $R \ln (K_{eq})$ versus

(18) Pate, J. E.; Ross, P. K.; Thamann, T. J.; Reed, C. A.; Karlin, K. D.; Sorrell, T. N.; Solomon, E. I. *J. Am. Chem. Soc.* **1989**, *111*, 5198.

Scheme II

Scheme III

$1/T$ (Figure 3B) gives the enthalpy and entropy of binding as tabulated in Table I.

The binding constant of azide to deoxy hemocyanin is a more difficult quantity to obtain. Azide is known to displace CO from deoxy hemocyanin and binds to the site.[19] This result was obtained from competition studies monitored by FTIR, and it was not possible to determine a binding constant based on these data. Azide binding to deoxy produces no detectable change in the optical absorption spectrum, and it is not possible to determine equilibrium concentrations of the species involved in a direct fashion. Thioacetamide (TA) has been shown[19] to reversibly bind to the deoxy protein to give an absorption band at 355 nm ($\epsilon \sim 4000$ M^{-1} cm^{-1}). Consequently, the thermodynamic parameters of azide binding to the deoxy protein were determined from the temperature dependence of the binding of TA and the competition of TA and azide for the deoxy hemocyanin site. The thermochemical cycle employed is given in Scheme II. In the scheme, K_1 is the azide binding constant, K_2 is the TA binding constant, and K_{sub} is the equilibrium constant for the competitive substitution of TA by N_3^-. From Scheme II it is apparent that $K_1 = K_2 K_{sub}$. K_2 was determined as described above (Figure 3C, upper curve), and the thermodynamic parameters for TA binding are given in Table I. K_{sub} was determined by monitoring the absorbance of deoxy-TA in a solution containing known initial concentrations of deoxy hemocyanin and both TA and N_3^- using the expression

$$K_{sub} = [\{[Hc]_0 - [HcTA] - [HcTA]/K_2([TA]_0 -$$
$$[HcTA])\}([TA]_0/[HcTA]) - 1\}]/\{[N_3^-]_0 - [Hc]_0 +$$
$$[HcTA] + [HcTA]/K_2([TA]_0 - [HcTA])\}$$

From a plot of $R \ln (K_{sub})$ versus $1/T$, ΔH_{sub} and ΔS_{sub} were determined (Figure 3C, lower curve, and Table I), and the enthalpy and entropy of azide binding to deoxy hemocyanin were calculated from $\Delta H_1 = \Delta H_2 + \Delta H_{sub}$ and $\Delta S_1 = \Delta S_2 + \Delta S_{sub}$. The values obtained are given in Table I.

The thermodynamic cycle in Scheme III relates the azide binding constants for each oxidation state to the standard reduction potentials of the azide bound forms relative to the aquo sites. For each ligand binding step $\Delta G_b = -RT \ln (K_{eq})$ and for each reduction (or oxidation) step $\Delta G_e = -nFE^\circ$. From Scheme III, the calculated differences in redox potentials for the azide derivatives relative to the aquo derivatives are given by

$$\Delta E^\circ = E^\circ(N_3^-) - E^\circ(\text{aquo}) = (RT/nF) \ln [K(\text{red})/K(\text{ox})]$$

(19) Hwang, Y. T. Ph.D. Dissertation, Massachusetts Institute of Technology, 1983.
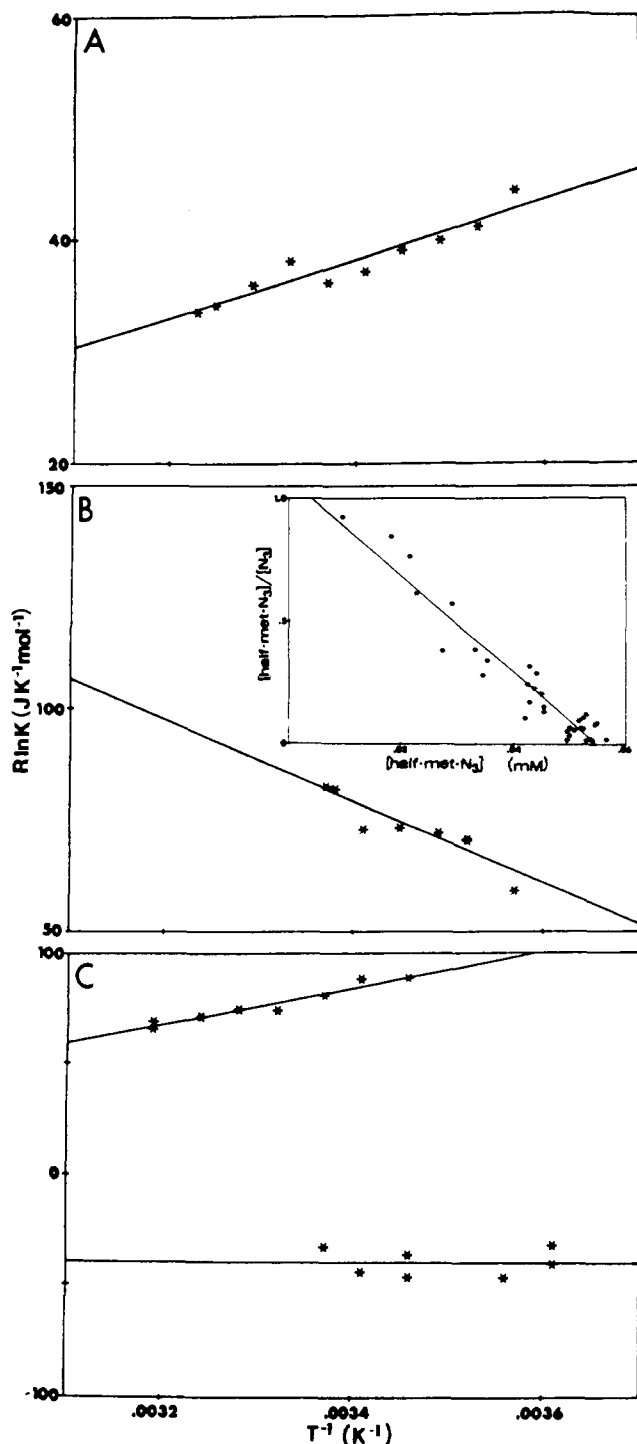
Figure 3. $R \ln K_{eq}$ vs $1/T$ plots for: (A) met-aquo + N_3^-, (B) half-met-aquo + N_3^- with (inset) a Scatchard plot at 23.5 °C, and (C) deoxy + thioacetamide (upper line) and the competitive substitution of thio-acetamide by N_3^- (lower line).

where K(red) is the azide binding constant for the reduced form in the couple and K(ox) is the corresponding binding constant for the oxidized form. The calculated values of ΔE° for the reduction of met to half-met and half-met to deoxy indicate that met-N_3^- is easier to reduce to half-met-N_3^- than met-aquo is to half-met-aquo by ~ 140 mV, half-met-N_3^- is harder to reduce than half-met-aquo by ~ 145 mV, and the overall reduction of met-N_3^- to deoxy-N_3^- is easier than that for the corresponding aquo derivatives by only ~ 3 mV. It is possible to calculate for these ΔE° values the relative equilibrium constants for the disproportionation reaction:
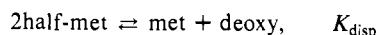
$$2\text{half-met} \rightleftharpoons \text{met} + \text{deoxy}, \qquad K_{disp}$$

$$K_{disp}(N_3^-)/K_{disp}(\text{aquo}) =$$
$$\exp[(nF/RT)(\Delta E^\circ(\text{half-met}/\text{deoxy}) -$$
$$\Delta E^\circ(\text{met}/\text{half-met}))] \approx 1.4 \times 10^{-5}$$

Thus half-met-N_3^- is between four and five orders of magnitude more stable than half-met-aquo with respect to disproportionation.

(B) **Spectroscopy.** Figure 4 presents the low-temperature (10 K) optical absorption, room-temperature circular dichroism (CD), and low-temperature (4.2 K) magnetic circular dichroism (LT-MCD) spectra for the series of half-met hemocyanins. Of particular note is the low-energy optical absorption band which is absent in half-met-NO_2^- but present in the other derivatives and shows both increasing intensity and a shift to lower energy down the series. In all the derivatives, another optical absorption is observed in the range 670–740 nm. Unlike the lower energy transition, the position of this band is not a strong function of the exogenous ligand. Further, for the Cl^-, Br^-, and I^- derivatives, the maximum molar absorptivity of this band is essentially constant ($\epsilon = 490$ M^{-1} cm^{-1}) and higher than that of half-met-NO_2^- by roughly a factor of 5. However, overlap with the lower energy intense absorption band complicates a quantitative comparison. The dominant feature in each of the CD spectra is a positive peak ($\Delta\epsilon = +0.67$ to $+1.45$ M^{-1} cm^{-1}) which shifts to lower energy by 20 nm from half-met-Cl^- to half-met-I^-. This peak does not directly correlate with either of the absorption bands. Similarly, the LT-MCD spectra show bands that appear to correlate with the CD peaks, but with the opposite sign. In the LT-MCD spectra presented in Figure 4 all temperature- and field-independent contributions (which account for less than 1% of the observed intensity at 4.2 K and 6.0 T) have been subtracted out and thus all bands are C terms.[20]

EPR spectra and simulations at X-, S-, and Q-band frequencies are shown in Figure 5. Relative to the X-band spectra, the Q-band spectra more clearly separate the $g_\parallel$ and $g_\perp$ regions but with a loss in the resolution of the hyperfine splittings. Conversely, the S-band spectra give better resolved hyperfine peaks, but overlapping $g_\parallel$ and $g_\perp$ regions. The X-, Q-, and S-band spectra were simulated using the powder pattern simulation program SIM14[21] (modified to include anisotropic line widths) with the Hamiltonian

$$H_{mag} = g_z\beta H_z \cdot S_z + g_y\beta H_y \cdot S_y + g_x\beta H_x \cdot S_x +$$
$$A_z^A(S_z \cdot I_z^A) + A_y^A(S_y \cdot I_y^A) + A_x^A(S_x \cdot I_x^A) +$$
$$A_z^B(S_z \cdot I_z^B) + A_y^B(S_y \cdot I_y^B) + A_x^B(S_x \cdot I_x^B)$$

The input parameters were the principal values of the g, A^A, and A^B tensors and effective widths in the H_x, H_y, and H_z field directions. The spectra were simulated based on hyperfine coupling to two $I_N = {}^3/_2$ nuclei. It is important to note that in the simulation program the principal directions of g, A^A, and A^B are constrained to be coincident. Simplex fitting procedures were moderately successful for the NO_2^- and Cl^- derivatives where the spectra show well-resolved simple features, but were not successful with the more complex spectra. Thus the half-met-Br^- and -I^- spectra were fit by inputting parameters and visually comparing the calculated and measured spectra. The criteria for a good fit were agreement between field positions for maxima and minima in the spectra and agreement of relative intensities of the features. For the NO_2^-, Cl^-, and Br^- derivatives good fits by both criteria were obtained. For half-met-I^- it was not generally possible to accurately reproduce the relative intensities of the features, but the field positions in the S- and Q-band spectra were reproduced relatively well. The origin of this discrepancy between the experimental and simulated half-met-I^- spectra is considered in detail in the Analysis section. The complete list of final parameters is given in the supplemental Tables S1–S4 and the values relevant to the

(20) (a) Stephens, P. J. *Adv. Chem. Phys.* **1976**, *35*, 197. (b) Piepho, S. B.; Schatz, P. N. *Group Theory in Spectroscopy*; Wiley-Interscience: New York, 1983.

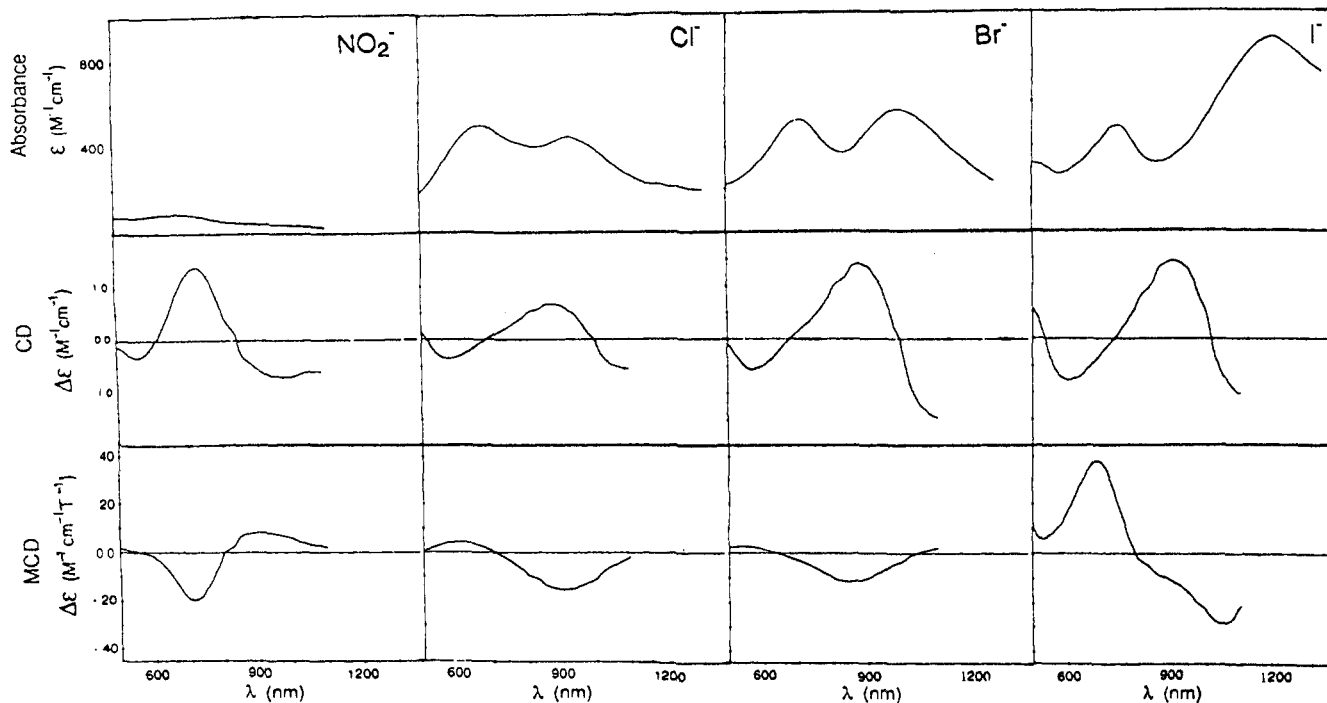(21) Lozos, G.; Hoffman, B.; Franz, C. Quantum Chemistry Program Exchange, No. 265.

Figure 4. Low-temperature (10 K) optical absorbance (top), room-temperature CD (middle), and low-temperature (4.2 K) MCD spectra (bottom) for the half-met series.
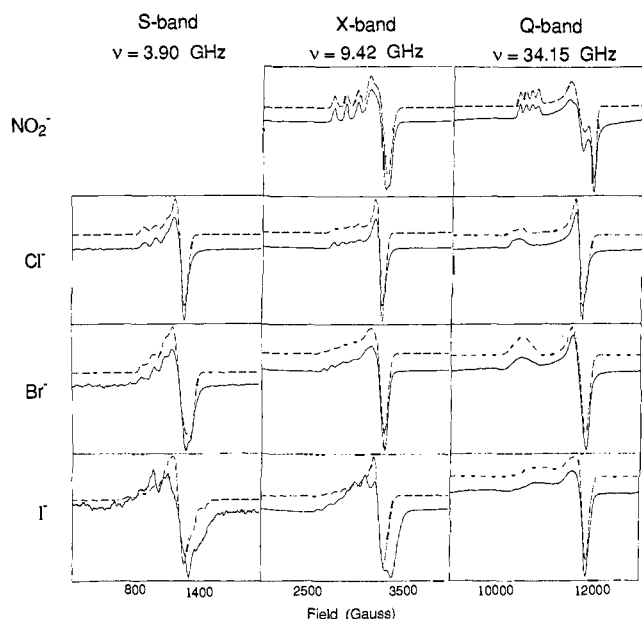

Figure 5. S-band (ν = 3.90 GHz, left), X-band (ν = 9.42 GHz, middle), and Q-band (ν = 34.15 GHz, right) EPR spectra for the half-met series (solid lines) and simulations (dashed lines) based on the parameters in Tables II and S1–S4.

analysis are summarized in Table II.

Electron spin–echo measurements were made to determine the shift in the EPR resonance frequency and thus the shift in g value upon application of an external electric field. Figure 6 shows the LEFE data for the series of half-met-L derivatives. In each spectrum, the shift parameter σ (units of V^{-1} cm), obtained for the electric field oriented parallel (E∥H) and perpendicular (E⊥H) to the magnetic field, is shown for magnetic field settings across the entire EPR spectrum. The positions of the g value turning points for each derivative are also indicated on the LEFE spectra. The half-met-NO$_2^-$ LEFE spectrum shows electric field induced shifts for both E∥H and E⊥H across the entire EPR spectrum, with the shifts for E∥H greater than those for E⊥H except near g_x and g_y. The weak modulation observed in the E∥H

Table II. EPR Simulation Parameters

| L	$g_\parallel$	$g_\perp$	$|A_\parallel^{Cu_A}|$ ($\times 10^{-4}$ cm^{-1})	$|A_\parallel^{Cu_B}|$ ($\times 10^{-4}$ cm^{-1})
NO$_2^-$	2.302	2.106, 2.041	132	<10[a]
Cl$^-$	2.347	2.078	96	<10[a]
Br$^-$	2.312	2.077	92	32
I$^-$	2.261	2.071	109	93

[a] Upper limit based on lack of resolution of this coupling in the EPR spectra.

shifts near $g_\parallel$ is possibly due to nuclear hyperfine interaction, but this modulation was not seen for any other half-met derivative. In comparison, the half-met-Cl$^-$ LEFE spectrum shows a quantitative decrease in the E∥H shift at $g_\parallel$; however, the magnitude of the E∥H shift between $g_\parallel$ and $g_\perp$ is not diminished, resulting in a large maximum in the E∥H spectrum at intermediate magnetic fields. There is negligible change in the E⊥H shift which is constant across the EPR spectrum. Comparing the LEFE spectra of the halide series, the E⊥H shifts are invariant across each spectrum and show a small decrease in magnitude down the series. To be noted, however, is the significant reduction of the E∥H shift maximum in the middle of the spectrum for half-met-Br$^-$ and the still greater reduction for half-met-I$^-$; the E∥H shift at $g_\parallel$ also decreases somewhat down the halide series.

Analysis

Excited States. Half-Met-NO$_2^-$: Ligand Field Assignments. The spectra of half-met-NO$_2^-$ in Figure 4 are very similar to those observed for simple monomeric tetragonal Cu(II) complexes.[22] Half-met-NO$_2^-$ is thus a Class I localized system and its absorption, CD, and LT-MCD spectra (combined in Figure 7) can be assigned based on monomeric Cu(II) selection rules. From the energies of the ligand field transitions (vide infra) and the g_z > $g_{x,y}$ > 2.00 EPR spectrum, the geometry of Cu$_A$(II) in the half-met-NO$_2^-$ site is best described as tetragonal with an $|x^2-y^2\rangle$ ground state. The fairly high intensity of the ligand field transitions, however, indicates that there is an additional odd parity component in the ligand field due to contributions from ligand-to-metal charge transfer (LMCT) states at higher energy. The highest effective symmetry for the d–d transitions is thus C_{4v} with

(22) Hathaway, B.; Billing, D. E. *Coord. Chem. Rev.* **1970**, *5*, 143.
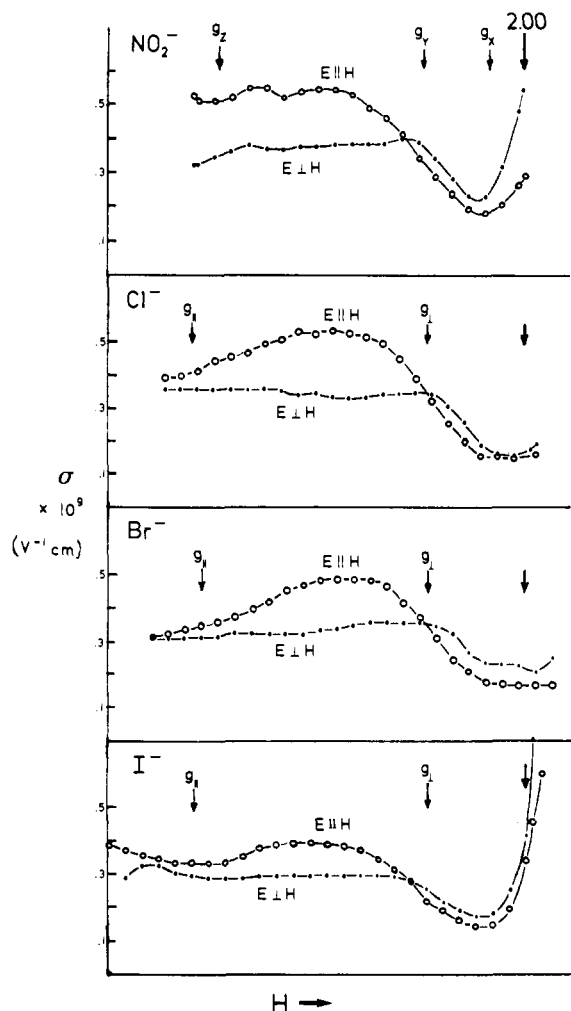
Figure 6. LEFE spectra of half-met-L, L = NO_2^- (ν = 9.610 GHz), Cl^- (ν = 9.562 GHz), Br^- (ν = 9.492 GHz), and I^- (ν = 9.448 GHz) where the experimental shifts, σ, for the E||H (O) and E⊥H (●) orientations are indicated at magnetic field settings across the EPR spectra. All spectra are aligned at g = 2.00, and the g values from the associated EPR spectra are indicated.
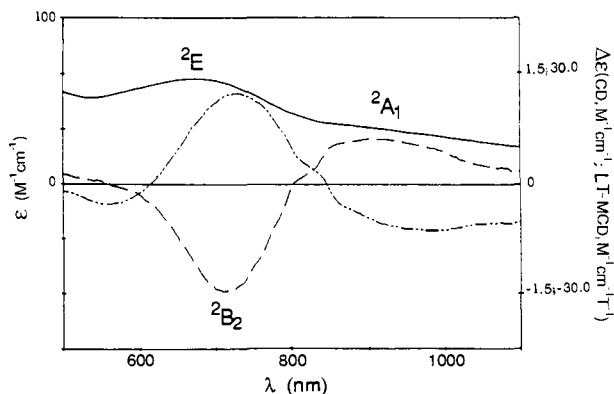
Figure 7. Low-temperature optical absorption (—), room-temperature CD (‑ ‑ ‑ ‑), and LT-MCD (‑ ‑ ‑) spectra for half-met-NO_2^- with assignments indicated.

the qualitative energy level diagram given in Figure 8. In the figure each state is labeled by the one-electron d orbital which gives the dominant contribution to the wave function of the unpaired electron. The ground state is $^2B_1$ and the excited state ordering shown is that appropriate to Cu(II) in a tetragonal site.

The only electric dipole allowed transition in a C_{4v} ligand field is $^2E \leftarrow {}^2B_1$, which should make the dominant contribution to the absorption spectrum. The relatively intense absorption feature at 680 nm can therefore be assigned as the $^2E \leftarrow {}^2B_1$ transition.
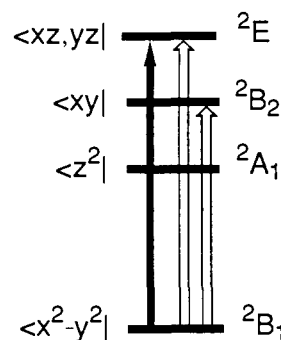
Figure 8. State diagram for a tetragonally distorted d^9 system with selection rules indicated: filled arrow, electric dipole allowed; open arrows, magnetic dipole allowed.

Additionally, there is a low-energy shoulder in the optical spectrum (λ_{max} = 910 nm, ϵ = 40 M^{-1} cm^{-1}). Based on comparison with monomeric tetragonal Cu(II) complexes,[22] the low-energy shoulder is assigned as excitation to the $^2A_1$ excited state which becomes allowed in symmetries lower than C_{4v}.

The selection rules for CD transition intensity require that the scalar product of the magnetic dipole and electric dipole transition moments be nonzero,[23] which is not possible in C_{4v} symmetry. However, both the $^2B_2 \leftarrow {}^2B_1$ and $^2E \leftarrow {}^2B_1$ transitions are magnetic dipole allowed and can gain CD intensity in lower symmetry ligand fields. $^2B_2 \leftarrow {}^2B_1$ has the largest value of the magnetic dipole transition moment[23] and is predicted to be most intense in the CD spectrum. The large positive peak in the half-met-NO_2^- CD spectrum can thus be assigned as the $^2B_2 \leftarrow {}^2B_1$ transition.

The expressions for an orientationally averaged MCD C term and the optical absorption transition intensity for an orbitally nondegenerate ground state are given in eq 3 and 4.[20]

$$\frac{\Delta A}{E} = \frac{\gamma \mu_B H}{kT} C_0 f(E) \tag{3a}$$

$$C_0 = \frac{-i}{3} \sum_{\alpha\alpha'\zeta} \langle G\alpha'|H_{zee}|G\alpha\rangle \cdot (\langle G\alpha|m|N\zeta\rangle \times \langle N\zeta|m|G\alpha'\rangle) \tag{3b}$$

$$A/E = \gamma D_0 f(E) \tag{4a}$$

$$D_0 = \frac{1}{3}\sum_{\alpha\zeta}|\langle G\alpha|m|N\zeta\rangle|^2 \tag{4b}$$

In eq 3 and 4, ΔA is the differential absorbance of left and right circularly polarized light, A is the total absorbance, γ is a collection of constants and concentration terms, μ_B is the Bohr magneton, H is the magnetic field strength, $f(E)$ is a band-shape function, and D_0 is the electric dipole strength of the transition. The sum in eq 3b is over all spin components of the ground (α,α') and excited (ζ) states, $H_{zee} = (L + 2.00S)$ is the Zeeman operator, and $m = er$ is the electric dipole operator. The eigenfunction $\langle G|$ represents the orbital ground state and $\langle N|$ represents an excited state. Equation 3b can be expanded as shown in eq 5, where the g_i ($i = x, y, z$) are the ground-state g tensor components and the m_i are electric dipole transition moments to excited state $\langle N|$, which indicates that net C term intensity depends on having transition intensity in two perpendicular directions.

$$C_0 \propto g \cdot (m \times m) = g_z m_x m_y + g_y m_x m_z + g_x m_y m_z \tag{5}$$

The most directly relevant parameter for the LT-MCD transitions is the ratio C_0/D_0 since this quantity does not depend on explicit values of the transition moment matrix elements.

From Figure 7 only the $^2E \leftarrow {}^2B_1$ transition has intensity in two directions (x, y). A treatment of the C term intensity requires that both spin–orbit coupling and low symmetry ligand field splitting be taken into account. Since at low temperature and high fields the $m_s = -^1/_2$ ground-state level is preferentially populated

---

(23) Yeh, C. Y.; Richardson, F. S. *Inorg. Chem.* **1976**, *15*, 682.

due to its lower energy, the basis set for the E state is chosen as $\{|\overline{xz}\rangle, |\overline{yz}\rangle\}$, where the bar denotes the $m_s = -1/2$ components. The interaction matrix for the perturbation $H' = \lambda L \cdot S + V_r$ within the ^2E state is given below.

H'	$|\overline{xz}\rangle$	$|\overline{yz}\rangle$
$\langle \overline{xz}|$	$\Delta_r/2$	$i\lambda/2$
$\langle \overline{yz}|$	$-i\lambda/2$	$-\Delta_r/2$

Δ_r is the rhombic splitting of the ^2E state due to the presence of a less than C_{4v} symmetry component in the ligand field potential, V_r, and λ is the spin–orbit coupling constant. Diagonalization of this matrix gives the eigenvalues, $W_\pm$, and wave functions, $|\bar{E}_\pm\rangle$, in eq 6 and 7.

$$W_\pm = \pm \frac{1}{2}(\Delta_r^2 + \lambda^2)^{1/2} \tag{6}$$

$$|\bar{E}_+\rangle = i\cos(\Theta/2)|\overline{xz}\rangle - i\sin(\Theta/2)|\overline{yz}\rangle \tag{7a}$$

$$|\bar{E}_-\rangle = -i\sin(\Theta/2)|\overline{xz}\rangle - i\cos(\Theta/2)|\overline{yz}\rangle \tag{7b}$$

In eq 7, Θ is given by $\tan(\Theta) = \lambda/\Delta_r$. Explicit evaluation of the matrix elements in eq 3b and 4b gives eq 8.

$$\frac{C_0(\bar{E}_+)}{D_0(\bar{E}_+)} = \frac{g_z \lambda}{2(\Delta_r^2 + \lambda^2)^{1/2}} \tag{8a}$$

$$\frac{C_0(\bar{E}_-)}{D_0(\bar{E}_-)} = \frac{-g_z \lambda}{2(\Delta_r^2 + \lambda^2)^{1/2}} \tag{8b}$$

From eq 8 it is apparent that two contributions to the MCD intensity are expected from the ^2E state. These contributions are equal in intensity, but opposite in sign and are centered at different energies. Thus the C terms for the two components of the ^2E state will tend to cancel to the extent that they overlap in energy. If the band-shape function, $f_{W_\pm}(E)$, for each component is taken as Gaussian with a half-width, Ω, centered at the appropriate energy ($W_\pm$, eq 6), then the total band shape can be expressed as in eq 9, where the sign of $f_{tot}(E)$ is opposite to that of λ.

$$f_{tot}(E) = \frac{C_0(\bar{E}_+)}{D_0(\bar{E}_+)} f_{W_+}(E) + \frac{C_0(\bar{E}_-)}{D_0(\bar{E}_-)} f_{W_-}(E) =$$
$$\mp \frac{g_z}{2(\Delta_r^2 + \lambda^2)^{1/2}} \exp\left\{ -\frac{4\ln(2)}{\Omega^2}(\Delta_r^2 + \lambda^2 + E^2) \right\} \times$$
$$\sinh\left\{ \frac{4\ln(2)}{\Omega^2}(\Delta_r^2 + \lambda^2)^{1/2} E \right\} \tag{9}$$

Equation 9 predicts a derivative-shaped pseudo-A term[20] centered at the ^2E peak energy. If $\lambda < 0$ ($\lambda_{Cu} = -828$ cm^{-1}), the positive contribution to the pseudo-A term occurs at higher energy. Clearly such signals are not apparent in the LT-MCD spectra in Figure 4. Equation 9 predicts that the net intensity of the pseudo-A term decreases with increasing Δ_r since the selection rule in eq 5 requires that an excited state have both $|\overline{xz}\rangle$ and $|\overline{yz}\rangle$ character for both m_x and m_y to be nonzero. From eq 7, as rhombic splitting increases, the excited-state wave functions become pure $|\overline{xz}\rangle$ or $|\overline{yz}\rangle$ and transition intensity is eliminated in one direction. Additionally, the net intensity decreases as Ω increases due to the combination of a lower peak height (for a fixed integrated intensity) and more extensive cancellation of the signals due to overlap. From eq 9 with reasonable values of Δ_r ($\approx 1.5\lambda$ to 2.0λ) and Ω (~ 5000 cm^{-1}) the net pseudo-A intensity is smaller by a factor of 10 relative to the C term intensity of a single axial component of the ^2E state. Thus the net C_0/D_0 ratio for the $^2E \leftarrow {}^2B_1$ transition is expected to be small and experimentally does not make the dominant contribution to the total LT-MCD spectrum as there is no pseudo-A term present in Figure 4.

The $^2B_2 \leftarrow {}^2B_1$, and $^2A_1 \leftarrow {}^2B_1$ transitions, while formally not allowed in C_{4v} symmetry, can gain C term intensity by spin–orbit coupling to the components of the ^2E state. This coupling also provides a mechanism for absorption intensity in these transitions. Based on a first-order mixing of ^2E character into the $^2B_2$ and

Table III. Ligand Field Assignments and Ligand Field Parameters for Half-Met-L

	L			
	NO$_2^-$	Cl$^-$	Br$^-$	I$^-$
$^2E \leftarrow {}^2B_1$				
Abs: E (cm^{-1})	14800	14830	14200	13540
ϵ_{max} (M^{-1} cm^{-1})	95	495	520	470
$E_{1/2}$ (cm^{-1})	5100	6800	5000	5200
D_0	0.18	1.2	0.99	0.98
$^2B_2 \leftarrow {}^2B_1$				
CD: E (cm^{-1})	13770	11490	11380	11150
$\Delta\epsilon$ (M^{-1} cm^{-1})	+1.37	+0.67	+1.41	+1.45
$E_{1/2}$ (cm^{-1})	2500	3200	3000	2500
LT-MCD: E (cm^{-1})	13680	11800	11100	9570
$\Delta\epsilon$ (M^{-1} cm^{-1} T^{-1})	−29.0	−11.1	−15.0	−27.5
$E_{1/2}$ (cm^{-1})	3050	3400	3300	3600
C_0	1.8×10^{-4}	1.8×10^{-5}	2.6×10^{-5}	5.5×10^{-5}
$^2A_1 \leftarrow {}^2B_1$				
Abs: E (cm^{-1})	10100			
ϵ_{max} (M^{-1} cm^{-1})	34			
$E_{1/2}$ (cm^{-1})	3800			
D_0	0.07			
Ds (cm^{-1})	275	370	325	310
Dt (cm^{-1})	390	330	330	320

$^2A_1$ excited states, the additional contributions to the C_0/D_0 ratios are given by eq 10.

$$C_0(B_2)/D_0(B_2) = -g_z/2 \tag{10a}$$

$$C_0(A_1)/D_0(A_1) = +g_z/2 \tag{10b}$$

From eq 10, the $^2B_2$ state has a negative MCD contribution and the $^2A_1$ has a positive contribution from excited-state spin–orbit coupling. The contributions to C_0 in eq 10a and 10b are not, however, necessarily equal in magnitude since, in general, $D_0(^2B_2) \neq D_0(^2A_1)$.

An additional factor in the LT-MCD spectral intensity pattern is spin–orbit coupling of excited states into the ground state. Mixing of the ^2E components into the $^2B_1$ ground state will give further MCD intensity to the $^2B_2$ and $^2A_1$ transitions due to nonzero $^2B_2 \leftarrow {}^2E$ and $^2A_1 \leftarrow {}^2E$ matrix elements. That such effects are important is evident from the experimental spectrum in Figure 7, which displays more negative than positive MCD intensity. Gerstman and Brill have shown[24] that if there is no mixing into the ground state, the principle of spectroscopic stability would require equal amounts of positive and negative MCD intensity. The mixing of ^2E character into the ground state gives the additional contributions in eq 11:

$$C_0'(B_2)/D_0'(B_2) = -g_z/2 \tag{11a}$$

$$C_0'(A_1)/D_0'(A_1) = +g_z/2 \tag{11b}$$

Again, the $^2B_2$ intensity is negative, while that of $^2A_1$ is positive. The absolute C term contributions once again depend on the values of D_0, which may be different for the two transitions. The relative D_0 values depend on the $^2B_2 \leftarrow {}^2E$ and $^2A_1 \leftarrow {}^2E$ electric dipole matrix elements and the energies of the ^2E components which mix into the ground state. In half-met-NO$_2^-$, the negative MCD contribution is from the $^2B_2 \leftarrow {}^2B_1$ transition and is larger than the positive contribution from the $^2A_1 \leftarrow {}^2B_1$ transition. Thus, while the ^2E MCD intensity is mostly canceled, the $^2B_2$ and $^2A_1$ transitions are reinforced by both intensity mechanisms. The assignments of the absorption, CD, and LT-MCD spectra of half-met-NO$_2^-$ are given in Figure 7 and summarized in Table III.

Half-Met-Halides: Ligand Field Assignments. Extending the analysis above to the half-met-Cl$^-$, -Br$^-$, and -I$^-$ derivatives, the band exhibited in the absorption spectrum of each at $\sim$700 nm is assigned as $^2E \leftarrow {}^2B_1$ based on its energy and the C_{4v} electric

(24) Gerstman, B. S.; Brill, A. S. *J. Chem. Phys.* **1985**, *82*, 1212.

dipole selection rules. The increase in absorption intensity for the $^2E \leftarrow {}^2B_1$ transition in the halide derivatives relative to half-met-NO_2^- is mostly related to overlap with the intense lower energy band, but there can be an additional contribution from mixing with relatively low-lying LMCT states. The CD spectrum for each derivative is dominated by a large positive peak which does not correlate with either the $^2E \leftarrow {}^2B_1$ transition or the low-energy absorption band. Based on the considerations discussed above for half-met-NO_2^-, these CD bands are assigned as the $^2B_2 \leftarrow {}^2B_1$ transition.

The LT-MCD spectra for half-met-Cl^- and -Br^- show a dominant negative contribution which correlates with the CD peak and is thus assigned as $^2B_2 \leftarrow {}^2B_1$. For half-met-I^- there is a large positive feature at ~ 680 nm in the LT-MCD spectrum. This band is ~ 1100 cm^{-1} higher in energy than the $^2E \leftarrow {}^2B_1$ transition in absorption and is therefore not likely directly associated with this state. The transition may be associated with a low-lying LMCT transition which is enhanced in MCD owing to the large spin–orbit coupling constant for I^-. The negative MCD peak at 1045 nm in this derivative is, however, assigned as the $^2B_2 \leftarrow {}^2B_1$ transition. Ligand field assignments for the half-met series are summarized in Table III.

Half-Met-Halides: IT Transition Assignments. For the half-met-Cl^-, -Br^-, and -I^- derivatives the intense absorption band at lowest energy cannot be assigned as a ligand field transition based on the analysis presented above for tetragonal Cu(II). It has previously been suggested[6] that this band could be an IT transition corresponding to the excitation of an electron from Cu(I) to Cu(II). This assignment was based on the absence of the band in the optical spectra of both the corresponding met-apo derivatives and the electronically localized half-met-xs-L derivatives. The alternative possible assignment of the low-energy band is as a ligand field transition associated with a fraction of the Cu(II) sites possessing a distorted tetrahedral geometry. Such sites would be expected to have ligand field transitions at significantly lower energies than the tetragonal sites and would have different EPR parameters which could account for the additional features in the X-band spectra. This possibility is, however, eliminated by the Q-band EPR data (Figure 5). The half-met-NO_2^- spectrum shows a clearly resolved rhombic splitting, but the other derivatives show axial symmetry and no detectable splitting of the $g_\perp$ region. If a mixture of both tetragonal and tetrahedral Cu(II) sites were present in, for example, half-met-I^-, then based on the two observed band energies and the predicted value[25] of $g_\perp = 2.00 - 2\lambda/E(^2E)$, a splitting of $g_\perp$(tetrahedral) $- g_\perp$(tetragonal) = 0.074 would be expected ($E(^2E)$ is the energy of the $^2E \leftarrow {}^2B_1$ transition). A difference of this magnitude would be easily resolvable in the Q-band spectrum (the rhombic splitting in half-met-NO_2^- is $g_y - g_x = 0.064$) but is not observed. Thus, the half-met sites can be regarded as spectroscopically homogeneous and the low-energy band cannot be assigned as a ligand field transition of Cu(II).

It is important to note that there is a general increase in the absorption intensity in the vis-NIR spectra of the half-met-halides relative to half-met-NO_2^- (Figure 4). However, the magnitude of the LT-MCD signal observed in this region is relatively constant. On a quantitative level the total D_0 values of the d–d and low-energy absorption bands increases by a factor of approximately 13 relative to half-met-NO_2^- while the C_0 intensity decreases by about 15%. Thus the increased absorption intensity which is mostly associated with the new low-energy band does not have a significant amount of LT-MCD intensity associated with it. Since D_0 increases, eq 4 requires that *at least* one m_i increase ($D_0 \propto \Sigma_i m_i^2$). However, no corresponding increase in C_0 is observed. Since all g values for the series are close to 2.00, eq 5 requires that for the low-energy transition *only* one m_i has intensity while the other two are essentially zero. This unidirectional polarization of the new feature is consistent with the predicted polarization of an IT band. Since the IT transition involves charge transfer from Cu_B to Cu_A, the electric dipole transition moment, $e(r_B - r_A)$, is directed only along the Cu–Cu axis. Such IT bands gain

(25) McGarvey, B. R. *Transition Met. Chem.* **1966**, *3*, 89.

Table IV. IT Parameters and Mixed-Valent Analysis for Half-Met-L

	L		
	Cl$^-$	Br$^-$	I$^-$
E_{IT} (cm^{-1})	10790	10010	8420
ϵ_{max} (M^{-1} cm^{-1})	415	560	1165
$E_{1/2}$ (cm^{-1})	2970	3015	3125
D_0	0.62	0.91	2.4
α^2_{opt}	5.4×10^{-3}	8.0×10^{-3}	2.0×10^{-2}
H_{AB} (cm^{-1})	790	895	1200
χ_{eff} (cm^{-1})	5300	5460	5870
ΔG°_{deloc} (J/mol)	0.34	0.54	1.42
ΔE_0 (cm^{-1})	5490	4550	2550
β_{eff}, (deg)	62	65	72

LT-MCD intensity only to the extent that they mix with ligand field bands with other polarizations, and significant MCD intensity in the IT region has thus far only been observed for completely delocalized Class III systems.[26] Lack of LT-MCD intensity confirms the earlier assignment of the lowest energy band in the half-met-halide series as an IT transition, and the parameters of the IT bands for the series are compiled in Table IV.

Ligand Field Analysis. The assignments given above indicate that, with the exception of the IT band, the visible and near-IR spectra of the half-met series are dominated by ligand field transitions associated with the Cu_A(II) center. From the assignments, the energy ordering of the states is $^2E > {}^2B_2 > {}^2A_1 \gg {}^2B_1$. Similar energy orderings are found for monomeric Cu(II) complexes with tetragonal ligand fields.[22] The ligand field energy expressions[27] for a square-planar d^9 system (approximated here as D_{4h}) are given in eq 12 where Ds and Dt are radial integrals which are treated as adjustable parameters.

$$E(^2E) = 18Ds + 25Dt \qquad E(^2A_1) = 24Ds + 10Dt$$
$$E(^2B_2) = 35Dt \qquad (12)$$

The values of Ds and Dt obtained by fitting the observed excited-state energies to eq 12 are included in Table III and are typical of those observed for monomeric tetragonal Cu(II) complexes.[28]

Mixed-Valent Analysis. The spectroscopic parameters of the IT bands for the half-met-halide series are given in Table IV. The ground state of a mixed-valent copper dimer can be described by a wave function of the form of eq 1 which expresses the delocalized ground-state electronic distribution in terms of localized wave functions. The mixing coefficient is α and the delocalization parameter α^2 represents the unpaired electron density on Cu_B. The Hush equations[9] relate the intensity parameters of an IT band to α^2 and to H_{AB}, the electronic coupling integral between the two localized states.

$$\alpha^2_{opt} = 4.24 \times 10^{-4} \epsilon_{max} E_{1/2}/(E_{max} R^2) \qquad (13a)$$

$$H_{AB} = \alpha E_{max} \qquad (13b)$$

In eq 13, ϵ_{max} is the molar absorptivity at the band maximum, $E_{1/2}$ is the half-width of the band, E_{max} is the energy of maximum absorption, and R is the distance in Å that the electron is transferred. In this analysis, R is taken as 3.5 Å based on Cu–Cu distances determined from EXAFS results for oxy hemocyanin (3.6 Å)[29a] and suggested for deoxy hemocyanin (3.4 Å).[29b] The values of α^2_{opt} and H_{AB} calculated from the IT parameters are given in Table IV. As the exogenous ligand is varied down the

(26) (a) Dubicki, L.; Ferguson, J.; Krausz, E. R.; Lay, P. A.; Maeder, M.; Magnuson, R. H.; Taube, H. *J. Am. Chem. Soc.* **1985**, *107*, 2167. (b) Dubicki, L.; Krausz, E. *Inorg. Chem.* **1985**, *24*, 4461. (c) Dubicki, L.; Ferguson, J.; Krausz, E. *J. Am. Chem. Soc.* **1985**, *107*, 179. (d) Dubicki, L.; Ferguson, J. *Chem. Phys. Lett.* **1984**, *109*, 128.
(27) (a) Companion, A. L.; Komarynsky, M. A. *J. Chem. Educ.* **1964**, *41*, 257. (b) Ds and Dt are related to α_2 and α_4 by $Ds = \alpha_2/21$ and $Dt = \alpha_4/21$.
(28) Wilcox, D. E.; Porras, A. G.; Hwang, Y. T.; Lerch, K.; Winkler, M. E.; Solomon, E. I. *J. Am. Chem. Soc.* **1985**, *107*, 4015.
(29) (a) Spiro, T. G.; Woolery, G. L.; Brown, J. M.; Powers, L.; Winkler, M. E.; Solomon, E. I. In *Biochemical and Inorganic Perspectives in Copper Coordination Chemistry*; Karlin, K., Ed.; Adenine Press: New York, 1983; p 23. (b) Kau, L. S.; Hodgson, K. O.; Solomon, E. I., to be published.
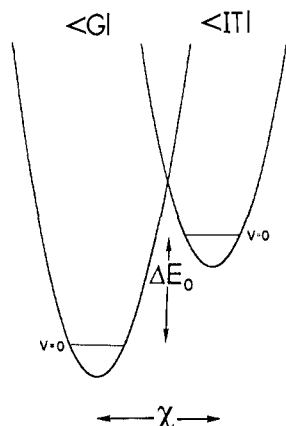
Figure 9. Potential surface diagram for a mixed-valent system, illustrating ΔE_0, the zero-point energy difference, and χ, the nuclear reorganizational energy.

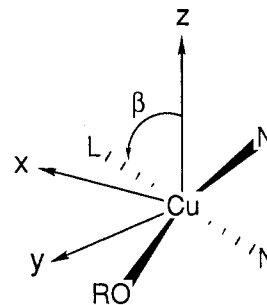**Figure 10.** Definition of the D_{2d} distortion angle, β, for $Cu_B(I)$ in the half-met site.

series, the values of both α^2 and H_{AB} increase; however, even for the most delocalized case (half-met-I^-) α^2 never rises above 0.02. The values reported are typical for Class II mixed-valent complexes interpreted within a Hush formalism.

The contribution of electronic delocalization to the comproportionation constant, K_{comp}, can be estimated from H_{AB} and E_{th}, the thermal barrier to intramolecular electron transfer.[30] K_{comp} is defined as the apparent equilibrium constant for the reaction met-L + deoxy-L $\rightleftharpoons$ 2half-met-L and is the reciprocal of the K_{disp} defined in the Results section. For symmetric mixed-valent systems with weak electronic coupling, $E_{th} \approx E_{max}/4$. For asymmetric sites, E_{th} is given by the more general expression $E_{th} \approx (E_{max})^2/4\chi$, where χ is the reorganizational energy, corresponding to the contribution of nuclear distortions to the observed transition energy.[11] The contribution of delocalization to the overall ΔG_{comp}, ΔG_{deloc}, is then given by $\Delta G_{deloc} = (H_{AB}/E_{max})^2\chi = \alpha^2\chi$.[30] The nuclear reorganization energy can be obtained from the temperature dependence of the half-width of the IT band.[9]

$$(E_{1/2})^2 = 8 \ln (2)\chi(\hbar\omega) \coth (\hbar\omega/2k_BT) \qquad (14)$$

In eq 14 $\hbar\omega$ is the effective frequency of the principal distorting mode. In neither the half-met-Cl^- nor the half-met-I^- derivative, which represent the extremes of delocalization, was any significant change in the optical absorption half-width observed between 10 K and the solvent melting point (~ 170 K). In order for the band to be independent of temperature below 170 K, it is required that the argument of the hyperbolic cotangent term be approximately 1.0 throughout this range. This constrains the effective frequency of the principal distorting mode to be ≥ 300 cm^{-1}. Based on this lower limit for the frequency and eq 14, upper limits for χ_{eff} for the half-met-halide series were calculated as given in Table IV. The fact that the values of χ_{eff} vary less than 6% among the derivatives indicates that structural distortions in the IT excited state of each derivative are similar. Based on the values of χ_{eff}, ΔG_{deloc} was calculated for each derivative and is given in Table IV. These values are comparable to those reported for other Class II mixed-valent dimers.[11,30] The contribution of delocalization to K_{disp} ($K_{disp} = K_{(deloc)}K'$, where K' is the portion due to all other factors) is given by $K_{(deloc)} = \exp(-\Delta G_{deloc}/RT) \approx 1.0$ from the values in Table IV and indicates that delocalization plays a negligible role in stabilizing the mixed-valent form relative to the fully oxidized or reduced sites.

An important trend in the half-met-L series is the shift in energy of the IT band. The energy of an IT band is generally expressed[11] as $E_{max} = \Delta E_0 + \chi$, where ΔE_0 is the energy difference between the $v = 0$ vibrational levels of the ground and IT state potential wells (Figure 9). Since the values of χ_{eff} are relatively constant, the origin of the shift in E_{max} is the zero-point potential well energy differences. The $Cu_A(II)$ site is tetragonal and therefore essentially

four coordinate. Previous chemical and spectroscopic studies on half-met hemocyanin[5,6] are consistent with the coppers being bridged by both the exogenous ligand, L (see Discussion), and an endogenous ligand, OR$^-$. For the Cu(I) site it is reasonable to assume that, in addition to the two bridging ligands, the two close (2 Å) histidines remain coordinated since they are present both in the deoxy structure and in the spectroscopically effective oxy site (Figure 1). Thus $Cu_B(I)$ can also be treated as four coordinate with ligands similar to those of $Cu_A(II)$. The origin of ΔE_0 is therefore most likely the energy difference between the $Cu_B(I)$ donor orbital and the $Cu_A(II)$ acceptor orbital. Since four-coordinate Cu(I) complexes tend to prefer tetrahedral or distorted tetrahedral geometries, this energy difference most likely arises from the difference in geometry at the $Cu_B(I)$ site. Thus the IT transition energy can be used to estimate ΔE_0 which provides a spectroscopic probe of the structure of the Cu(I) site and its variation in the half-met series. Ligand field theory can be used to calculate the energy differences between the $Cu_B(I)$ donor orbitals and the half-filled $|x^2-y^2\rangle$ acceptor orbital on tetragonal $Cu_A(II)$. This energy difference is an estimate of ΔE_0 and is a sensitive function of the $Cu_B(I)$ geometry and can thus be compared with the experimental ΔE_0 values for the half-met-L series to obtain estimates of the effective geometry of $Cu_B(I)$.

The model for the Cu(I) site is taken to be between limiting square-planar ($\beta = 90°$) and tetrahedral ($\beta = 54°$) geometries which are related by a D_{2d} distortion defined in Figure 10. The energies of the Cu(I) d orbitals are independent of the Cu–L–Cu angle θ and depend only on the coordinates of the ligands in the coordinate system of the metal. The energy of each d orbital (and therefore, each state) can be calculated as a function of geometry by the ligand field expressions given below.[27]

$$E(^2B_1;x^2-y^2) = 12(3 \cos^2 \beta - 1)Ds - (35 \sin^4 \beta + \delta)Dt/2$$

$$E(^2B_2;xy) = 12(3 \cos^2\beta - 1)Ds + (35 \sin^4 \beta - \delta)Dt/2$$

$$E(^2A_1;z^2) = -12(3 \cos^2 \beta - 1)Ds - 3\delta Dt$$

$$E(^2E;xz,yz) = -6(3 \cos^2 \beta - 1)Ds + 2\delta Dt$$

where

$$\delta = 35 \cos^4 \beta - 30 \cos^2 \beta + 3$$

For these calculations Ds (335 cm^{-1}) and Dt (325 cm^{-1}) are averages over the values for half-met-Cl^-, -Br^-, and -I^- given in Table III. This procedure assumes that the Ds and Dt values appropriate to $Cu_A(II)$ in the ground state are transferable to Cu_B in the IT excited state. Orbital splittings for Cu(I) are generally significantly smaller than those of Cu(II) in comparable ligand fields. However, an appropriate electronic description of the IT transition requires the final state to correspond to the electronically relaxed IT state. Thus in the IT transition the d-orbital splittings of Cu_A decrease while the splittings of Cu_B increase to those appropriate for Cu(II) in the Cu_B geometry.

The calculated energies of each Cu_B d orbital in the IT excited state are displayed as a function of β in Figure 11. In the figure, the zero of energy is the energy of the $|x^2-y^2\rangle$ orbital of Cu_A in the ground state. Thus, if both coppers are square planar ($\beta = 90°$), ΔE_0 for transfer of an electron from the $|x^2-y^2\rangle$ orbital of

(30) (a) Sutton, J. E.; Sutton, P. M.; Taube, H. *Inorg. Chem.* **1979**, *18*, 1017. (b) Sutton, J. E.; Taube, H. *Inorg. Chem.* **1981**, *20*, 3125.

6116   *J. Am. Chem. Soc., Vol. 111, No. 16, 1989*

Westmoreland et al.
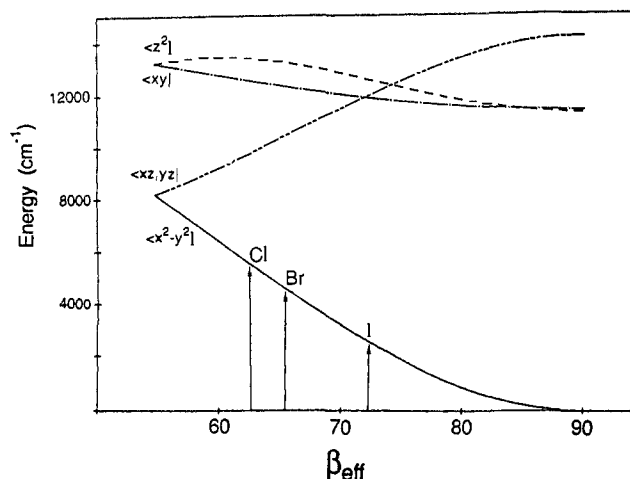
Figure 11. Ligand field energy diagram for $Cu_B(I)$ as a function of distortion angle, β. The levels are labeled by the orbital which contains the unpaired electron and the energies corresponding to ΔE_0 for half-met-Cl^-, -Br^-, and -I^- are indicated.

Figure 12. Definition of the structure angles θ and ρ for the site.

Cu_B to the $|x^2-y^2\rangle$ orbital of Cu_A is zero. With this definition of $E = 0$, ΔE_0 for half-met-L is approximately the energy of the Cu_B donor orbital at the appropriate value of β.

There are four possible IT transitions, corresponding to the four different $Cu_B(I)$ donor orbitals. Since charge-transfer intensity is proportional to the square of donor–acceptor orbital overlap, the dominant IT band will be the one with the largest value of this overlap. The metal–metal distance is too large for effective direct overlap; thus the mechanism must be through a bridging ligand. The total overlap is the sum of the σ overlap and the π overlap of the Cu(I) orbital with the $|p_x\rangle$ orbital of the bridging atom which has the best overlap with the $Cu_A|x^2-y^2\rangle$ accepting orbital. This overlap may be calculated quantitatively in terms of an angular overlap model.[31] The expressions for the overlap in terms of the structural parameters defined in Figure 10 are:

$$S^2_{tot}(j) = (-\cos\theta \, \Sigma_\sigma(j)S_\sigma + \sin\theta \, \Sigma_\pi(j)S_\pi)^2$$

$$\Sigma_\sigma(x^2-y^2) = \left(\sqrt{3}/4\right)[1 - \cos(2\beta)]$$

$$\Sigma_\pi(x^2-y^2) = -\sin\beta\sin(2\beta)\,Z/2$$

$$\Sigma_\sigma(xy) = 0$$

$$\Sigma_\pi(xy) = \sin\beta\,Z$$

$$\Sigma_\sigma(z^2) = [1 + 3\cos(2\beta)]/4$$

$$\Sigma_\pi(z^2) = \sqrt{3}\sin\beta\sin(2\beta)\,Z/2$$

$$\Sigma_\sigma(xz) = \sqrt{3}\sin(2\beta)/2$$
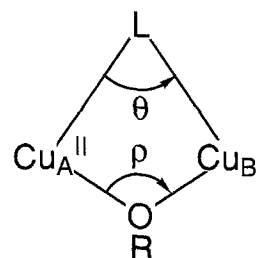
$$\Sigma_\pi(xz) = -\sin\beta\cos(2\beta)\,Z$$

$$\Sigma_\sigma(yz) = 0$$

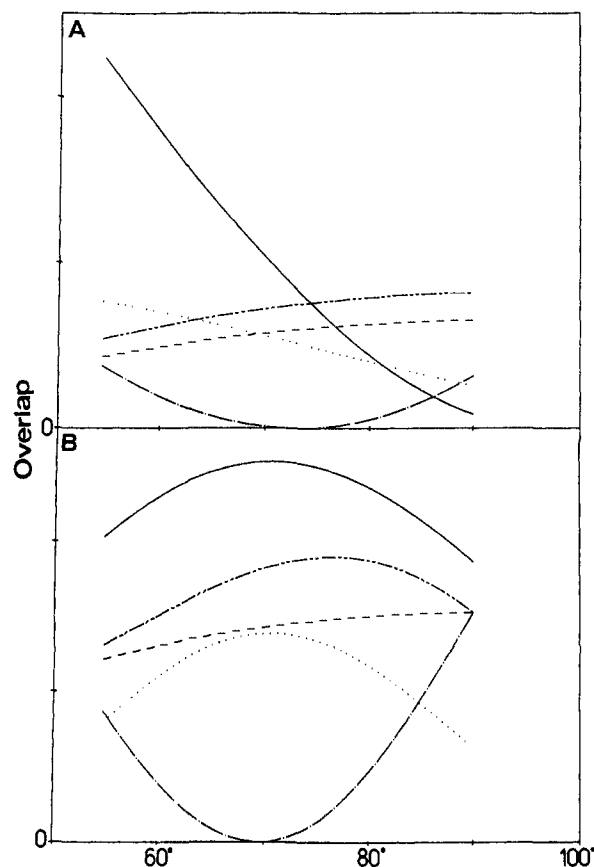$$\Sigma_\pi(yz) = [\cos\beta - \sin\beta\cos(2\beta)]Z$$

where

$$Z = (1 + \sin^2\beta)^{-1/2}$$

The value of θ for each derivative was estimated based on calculated angles from crystallographically determined average bond lengths for a variety of halogen bridged Cu(II) and Cu(I) dimers. The model and parameters are given in Figure 12 and Table V. It was assumed that the endogenous bridge is adequately represented by parameters for bridging oxygen and that the L⋯OR distance is essentially the sum of the L and O covalent radii. The values of the S_σ and S_π overlap integrals were estimated as an average of calculated values for Cu–Cl and Cu–Br.[32]

Figure 13. S^2_{tot} for the $L_{(exo)}$ $|p_x\rangle$ orbital with each d orbital on $Cu_B(I)$ vs angle for the half-met site: (A) as a function of θ for $\beta = 66°$; (B) as a function of β for $\theta = 70°$. The orbitals are $|x^2-y^2\rangle$ (—), $|xy\rangle$ (---), $|z^2\rangle$ (⋯), $|xz\rangle$ (-----), and $|yz\rangle$ (-·-·).
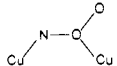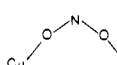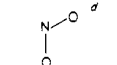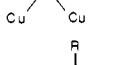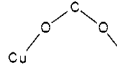
The overlaps are a very sensitive function of θ. In Figure 13A are plotted the calculated $S^2_{tot}(j)$ for each donor orbital as a function of θ at constant $\beta = 66°$. At $\theta = 90°$ the π overlap of $Cu_B|yz\rangle$ with $|p_x\rangle$ is dominant since the $Cu_B|x^2-y^2\rangle$ and $|p_x\rangle$ orbitals are nearly orthogonal. As θ decreases, σ overlap of $Cu_B|x^2-y^2\rangle$ with $|p_x\rangle$ increases dramatically and at $\theta = 70°$ is the largest overlap. The overlaps are also a function of β, and Figure 13B shows the overlap as a function of the distortion β for $\theta = 70°$, which is the mean of this structural parameter for Cl^-, Br^-, and I^-. With this value of θ, the $Cu_B|x^2-y^2\rangle$ orbital has the highest overlap with $|p_x\rangle$ for $54° < \beta < 90°$. Thus the donor orbital for the IT transition appears to be the $Cu_B|x^2-y^2\rangle$ orbital based on its predicted maximum intensity.

Correlating the observed ΔE_0 (Table IV) with the calculated energy difference of the $Cu_B|x^2-y^2\rangle$ orbital in Figure 11 as a function of β, it is possible to estimate β_{eff}, which defines the spectroscopically effective geometry of the four-coordinate $Cu_B(I)$ site. The estimated values of β_{eff} are tabulated in Table IV. The results indicate that β_{eff} varies over a range of $\sim10°$ with half-met-Cl^- being within about $8°$ of tetrahedral. The trend down

---

(31) Larsen, E.; La Mar, G. N. *J. Chem. Educ.* **1974**, *51*, 633.

(32) Smith, D. W. *J. Chem. Soc. A* **1970**, 1498.

Table V. Estimated Structural Parameters for Half-Met-L

L	Cu(II)-L (Å)[a]	Cu(I)-L (Å)[a]	θ[b]	ρ[b]
O	1.96	2.00		
Cl	2.46	2.42	76°	99°
Br	2.64	2.56	72°	102°
I	3.01	2.63	67°	105°
[structure: Cu–N–O bridging, N bonded to O]	1.30 (Cu-O)	2.02 (Cu-N)		101°
[structure: N bridging with two O to Cu]	2.23[c]	2.35		111°
[structure: N with two O, bridging two Cu]	2.13[d]	2.17		106°
[structure: R–C with two O bridging two Cu]	2.29	2.34		110°
[structure: R–C=O with O bridging two Cu]	2.08	2.12		102°

[a] Average bond distances based on a search of the Cambridge Structure Database. [b] Calculated based on the average bond distances and Figure 12, assuming that the O–L distance is the sum of the O and L covalent radii. [c] Based on parameters for nitrate complexes. [d] Based on parameters for R–NO$_2$ complexes.

the series follows the trend in delocalization and shows that as Cu$_B$(I) gains more Cu(II) character (α^2 increases), it distorts toward a more tetragonal geometry ($\beta_{eff} \rightarrow 90°$). Thus the geometries of both the Cu(II) and Cu(I) in the half-met sites have been estimated from the ligand field and IT excited-state spectral features, respectively.

Ground State. The EPR spectra for the half-met series and simulations (Figure 5) show variations in $g_\parallel$ and $A_\parallel$ as summarized in Table II. It is important to determine the role delocalization plays in determining the ground-state magnetic properties of a mixed-valent dimer. The dimer **g** tensor can be related to the local Cu$_A$ and Cu$_B$ **g** tensors. Additionally, since the hyperfine coupling parameters are a function of unpaired spin density at the nucleus, they should provide an estimate of delocalization which is independent of the IT absorption band analysis. The LEFE data also show trends which correlate with delocalization and constitute an important probe of the ground-state wave function.

Half-Met-NO$_2$⁻. Half-met-NO$_2$⁻ represents the Class I localized limit and therefore should be analyzed in terms of a monomeric tetragonal Cu(II) site. However, a rhombic splitting is apparent in the Q-band spectrum and indicates lower than axial symmetry at the site. In symmetries lower than C_{4v} the $|z^2\rangle$ orbital transforms under the same irreducible representation as $|x^2-y^2\rangle$ and thus can contribute to the ground-state wave function, $|G\rangle = \xi(p|x^2-y^2\rangle + q|z^2\rangle)$ where $p^2 + q^2 = 1.0$ and ξ^2 is the total metal character in the ground state. The extent of this $|z^2\rangle$ mixing can be determined quantitatively from the observed rhombic splittings using the expression[33]

$$\xi^2 q^2 = (12 - R_g^2 - 6(4 - R_g^2)^{1/2})/2(12 - R_g^2)$$

where $R_g = 2(\Delta g_y - \Delta g_x)/(\Delta g_y + \Delta g_x)$, $\Delta g_y = g_y - 2.00$, and $\Delta g_x = g_x - 2.00$. For half-met-NO$_2$⁻ the splitting is quantitatively accounted for with $\xi^2 q^2 = 2.1\%$ $|z^2\rangle$ character in the ground state.

Half-met-NO$_2$⁻ exhibits a normal tetragonal Cu(II) parallel hyperfine pattern except that the hyperfine coupling constant is somewhat smaller than expected for a tetragonal Cu(II) site ($|A_z| = 132 \times 10^{-4}$ cm⁻¹). Since A_z is generally a negative number for

tetragonal Cu(II), A_z is taken as -132×10^{-4} cm⁻¹. Expressions for the g_z and A_z values of a low-symmetry distorted Cu(II) site are given in eq 15.[33]

$$g_z = 2.00 - \frac{8\lambda\xi^2 p^2 \varphi^2}{E(^2B_2)} \tag{15a}$$

$$A_z = P_d\left[\kappa - \frac{4}{7}\xi^2(p^2 - q^2) + \frac{(3p - 3^{1/2}q)}{14(p + 3^{1/2}q)}\Delta g_y + \frac{(3p + 3^{1/2}q)}{14(p - 3^{1/2}q)}\Delta g_x + \Delta g_z\right] = A_F + A_S + A_L \tag{15b}$$

In eq 15 φ^2 is the metal character of the $^2B_2$ state and is estimated as $\varphi^2 = 1.1\xi^2$.[33b] $P_d\kappa$ is the Fermi contact contribution to the hyperfine, A_F; the term in ξ^2 is the spin dipolar contribution, A_S; the terms in Δg are orbital dipolar contributions, A_L. The value of P_d from Hartree–Fock calculations of copper atoms is 396 $\times$ 10⁻⁴ cm⁻¹.[34] The most direct measure of electron density at the nucleus is the Fermi contact term, $A_F = A_z - A_S - A_L$. As described above, the rhombic splitting of the $g_\perp$ region of the EPR spectrum gives the net $|z^2\rangle$ character $\xi^2 q^2 = 0.021$. Equation 15a and the experimental g_z and $E(^2B_2)$ values give the net $|x^2-y^2\rangle$ character, $\xi^2 p^2 = 0.745$. From these results it is possible to calculate $p^2 = 0.973$, $q^2 = 0.027$, and $\xi^2 = 0.766$. Inserting these values into eq 15b with the experimental g value shifts and $A_z^{Cu_A}$, A_S and A_L can be calculated, yielding $A_F^{Cu_A} = -100 \times 10^{-4}$ cm⁻¹ for half-met-NO$_2$⁻. Since no hyperfine coupling to Cu$_B$ was resolved, it is not possible to obtain $A_F^{Cu_B}$ by this method, but it can be estimated to be $|A_F^{Cu_B}| \leq 6 \times 10^{-4}$ cm⁻¹ by comparison to half-met-Cl⁻ as discussed below.

Half-Met-Halides: g Values. The EPR spectra for half-met-Cl⁻, -Br⁻, and -I⁻ (Figure 5) show axially symmetric patterns at all frequencies, and the EPR parameters (Table II) are a function of the exogenous ligand with the value of $g_\parallel$ showing significant variations down the series. In order to understand the contribution of delocalization to the ground-state magnetic parameters, it is necessary to relate the **g** tensor of the dimer to the **g** tensors of each copper center. Spin–orbit coupling mixes excited-state orbital angular momentum into the ground state and causes anisotropic deviations from $g = 2.00$. Quantitatively the **g** tensor for an orbitally nondegenerate $S = 1/2$ system is given by[35]

$$\mathbf{g} = (2.00)\mathbf{1} + 2\mathbf{\Lambda} \tag{16a}$$

where **1** is the unit tensor and

$$\Lambda_{ij} = -\sum_N \langle G|L_i'|N\rangle\langle N|L_j|G\rangle(E_N - E_G)^{-1} \tag{16b}$$

L_j is the jth component of the orbital angular momentum operator and $L_i' = \sum_k \lambda_k L_i^k$. The sum over N in eq 16b is over all excited states and λ_k is the spin–orbit coupling parameter for atom k. Note that the origin for the L_i' operator is at atom k, whereas the origin for L_i is a suitably chosen molecular origin. The ground-state wave function of the dimer may be written as

$$|G\rangle = a|Cu_A\rangle + b|Cu_B\rangle + c|L_{(exo)}\rangle + d|L_{(endo)}\rangle \tag{17}$$

where $|L_{(exo)}\rangle$ are the exogenous ligand orbitals and $|L_{(endo)}\rangle$ represents the contributions of all other ligands. $L_{(exo)}$ is treated separately since for $L_{(exo)} = Br⁻$ and I⁻ the ligand spin–orbit coupling parameters are large enough to influence the molecular g values.

There are several coordinate systems involved in evaluating the matrix elements of eq 16. The "molecular" coordinate system (x_m, y_m, z_m) is the one in which the **g** tensor is diagonal and directly corresponds to the physical observables (i.e., $g_\parallel$ and $g_\perp$ in Table II). There is also a local coordinate system for each atom which is the coordinate system in which its ligand field is diagonal. For tetragonal Cu$_A$, z_A is perpendicular to the equatorial plane, x_A lies in the plane along the Cu$_A$–L$_{(exo)}$ bond, and y_A is defined by

(33) (a) Hitchman, M. A.; Olson, C. D.; Belford, R. L. *J. Chem. Phys.* **1969**, *50*, 1195. (b) Gewirth, A. A.; Cohen, S. L.; Schugar, H. J.; Solomon, E. I. *Inorg. Chem.* **1987**, *26*, 1133.

(34) Freeman, A. L.; Watson, R. E. In *Magnetism*; Rado, G., Suhl, H., Eds.; Academic Press: New York, 1965; Vol. 2A, p 167.

(35) Solomon, E. I. *Comments Inorg. Chem.* **1984**, *3*, 225.
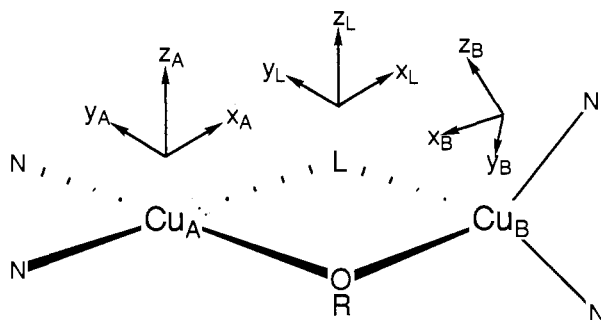
Figure 14. The spectroscopically effective half-met-L active site with the local coordinate systems at each center indicated.

$x_A \times y_A = z_A$. At the exogenous ligand, $x_{L(exo)}$ is chosen to be colinear with x_A, and $y_{L(exo)}$ and $z_{L(exo)}$ are parallel to y_A and z_A, respectively. For Cu_B, the local D_{2d} symmetry axis is taken as z_B, and the x_B and y_B axes lie in the mirror planes (with x_B in the same plane as the Cu_B–$L_{(exo)}$ bond) and obey an $x_B \times y_B = z_B$ relation. These coordinates are included in Figure 14. Once these four coordinate systems have been defined, the L_i matrix elements of eq 16 must be evaluated with respect to a single fixed coordinate system (x_m, y_m, z_m), while the L_i' elements are evaluated in local atomic coordinates. All the coordinate systems are related by translations and unitary rotations. It is most convenient to compute the matrix elements in the Cu_A coordinate system and diagonalize the resulting g^2 tensor (eq 16a) to give the principal g values and the rotations relating (x_m, y_m, z_m) to (x_A, y_A, z_A) and (x_B, y_B, z_B).

Since $L_{(exo)}$ and Cu_B are not centered at the origin in the Cu_A coordinate system, L_i operating on $|L_{(exo)}\rangle$ and $|Cu_B\rangle$ will generate additional terms due to the translation and rotation of the local coordinates relative to those of the origin.[20b] The coordinate system at $L_{(exo)}$ is related to the Cu_A coordinates by:

$$x_A = x_L - R_{AL(exo)}$$

$$y_A = y_L$$

$$z_A = z_L$$

where $R_{AL(exo)}$ is the vector from Cu_A to $L_{(exo)}$. For Cu_B the transformations involve rotating the Cu_B coordinates into parallel with Cu_A and then translation to the Cu_A origin by R_{AB}. The rotation is given by $(90 - \beta)$ about x_B, then about y_B by τ where $\sin \tau = (1 + \cos^2 \beta)^{-1/2}$.

$$x_A = x_B \sin \beta + z_B \cos \beta - R_{AB} \sin \theta$$

$$y_A = -x_B \cos \beta \sin \tau + y_B \cos \tau + z_B \sin \beta \sin \tau - R_{AL(exo)} + R_{BL(exo)} \cos \theta$$

$$z_A = -x_B \cos \beta \cos \tau - y_B \sin \tau + z_B \sin \beta \cos \tau \quad (18)$$

The angular momentum operators at $L_{(exo)}$ and Cu_B can now be defined in terms of the Cu_A coordinate system. For $L_{(exo)}$,

$$L_{z(A)} = -i\hbar(x_A \partial/\partial y - y_A \partial/\partial x)$$
$$= -i\hbar(x_{L(exo)} \partial/\partial y - y_{L(exo)} \partial/\partial x - R_{AL(exo)} \partial/\partial y)$$
$$= L_{z(L(exo))} + i\hbar R_{AL(exo)} \partial/\partial y$$

$$L_{y(A)} = -i\hbar(z_A \partial/\partial x - x_A \partial/\partial z) = L_{y(L(exo))} - i\hbar R_{AL(exo)} \partial/\partial z$$

$$L_{x(A)} = -i\hbar(y_A \partial/\partial z - z_A \partial/\partial y) = L_{x(L(exo))}$$

where $L_{i(L(exo))}$ implies the L_i operation carried out about center $L_{(exo)}$. For Cu_B, the values are computed from eq 19 as

$$L_{x(A)} = \cos \tau \ (L_{x(B)} + i\hbar(R_{AL(exo)} \cos \theta - R_{BL(exo)})) \partial/\partial z)$$
$$+ \cos \beta \sin \tau \ (L_{y(B)} - i\hbar R_{AL(exo)} \sin \theta \partial/\partial z)$$
$$- \sin \beta \sin \tau \ (L_{z(B)} + i\hbar(R_{BL(exo)} - R_{AL(exo)}\cos \theta) \partial/\partial x$$
$$+ i\hbar R_{AL(exo)} \sin \theta \partial/\partial y)$$

$$(19a)$$

$$L_{y(A)} = \sin \beta \ (L_{y(B)} - i\hbar R_{AL(exo)} \sin \theta \partial/\partial z)$$
$$+ \cos \beta \ (L_{z(B)} + i\hbar(R_{BL(exo)} - R_{AL(exo)}) \cos \theta) \partial/\partial x$$
$$+ i\hbar R_{AL(exo)} \sin \theta \partial/\partial y)$$

$$(19b)$$

$$L_{z(A)} = \sin \tau \ (L_{x(B)} + i\hbar(R_{AL(exo)} \cos \theta - R_{BL(exo)}) \partial/\partial z)$$
$$- \cos \beta \cos \tau \ (L_{y(B)} - i\hbar R_{AL(exo)}\sin \theta \partial/\partial z)$$
$$+ \sin \beta \cos \tau \ (L_{z(B)} + i\hbar(R_{BL(exo)} - R_{AL(exo)} \cos \theta) \partial/\partial x$$
$$+ i\hbar R_{AL(exo)} \sin \theta \partial/\partial y)$$

$$(19c)$$

Using these expressions, the matrix elements of L_i in eq 16 can be computed. Since terms containing $\partial/\partial x$, $\partial/\partial y$, and $\partial/\partial z$ are nonzero only with p/d and s/p mixing, they represent relatively small contributions to the total orbital angular momentum and are neglected. The expressions which result are independent of metal–ligand and metal–metal distances and the M–L–M angle. Equation 19 can be substituted in eq 16b to obtain the Λ_{ij} which are most conveniently expressed in terms of the local Cu and $L_{(exo)}$ contributions to the g values:

$$\Lambda_{xx} = a^2 \Delta g_\perp{}^{(A)} + b^2[\sin^2 \beta \sin^2 \tau \ \Delta g_\parallel{}^{(B)} + (\cos^2 \tau + \cos^2 \beta \sin^2 \tau)\Delta g_\perp{}^{(B)}] + c^2 \Delta g_\perp{}^{(L(exo))}$$

$$\Lambda_{xy} = b^2[-\sin \beta \cos \beta \sin \tau \ \Delta g_\parallel{}^{(B)} + \sin \beta \cos \tau \ \Delta g_\perp{}^{(B)}]$$

$$\Lambda_{xz} = b^2[-\sin^2 \beta \sin \tau \cos \tau \ \Delta g_\parallel{}^{(B)} + \sin\tau \cos \tau \ (1 - \sin \beta \cos \beta)\Delta g_\perp{}^{(B)}]$$

$$\Lambda_{yy} = a^2 \Delta g_\perp{}^{(A)} + b^2[\cos^2 \beta \ \Delta g_\parallel{}^{(B)} + \sin^2 \beta \ \Delta g_\perp{}^{(B)}] + c^2 \Delta g_\perp{}^{(L(exo))}$$

$$\Lambda_{yz} = b^2[\sin \beta \cos \beta \ \Delta g_\parallel{}^{(B)} + \sin \beta \sin \tau \ \Delta g_\perp{}^{(B)}]$$

$$\Lambda_{zz} = a^2 \Delta g_\parallel{}^{(A)} + b^2[\sin^2 \beta \cos^2 \tau \ \Delta g_\parallel{}^{(B)} + (\sin^2 \tau + \cos^2 \beta \cos^2 \tau)\Delta g_\perp{}^{(B)}] + c^2 \Delta g_\parallel{}^{(L(exo))} \quad (20a)$$

where

$$\Delta g_\parallel{}^{(A,B)} = -(1.1\xi^4)8\lambda_{A,B}/E(^2B_2)$$

$$\Delta g_\perp{}^{(A,B)} = -(1.1\xi^4)2\lambda_{A,B}/E(^2E)$$

$$\Delta g_\parallel{}^{(L(exo))} = \Delta g_\perp{}^{(L(exo))} = -(1.1c^4)2\lambda_{L(exo)}/E(LMCT) \quad (20b)$$

The factor of 1.1 again arises from the fact that the excited states which spin–orbit couple to the ground state are estimated to be approximately 10% less covalent than the ground state,[33b] and ξ^2 in this context refers to the total metal character in the ground-state wave function. In order to calculate the **g** tensor in eq 16, the observed ligand field energies of Cu_A and the LMCT energies for half-met-Br$^-$ and I$^-$ were used. The ligand field energies for Cu_B were estimated from Figure 11 with the appropriate β for each half-met-L. The spin–orbit coupling constants were taken as $\lambda_{Cu} = -828$ cm^{-1}, $\lambda_{Br} = -2460$ cm^{-1}, $\lambda_I = -5065$ cm^{-1}. For half-met-Cl$^-$, -Br$^-$, and -I$^-$, the **g**^{2} tensor was diagonalized and the values of a^2, b^2, and c^2 from $|G\rangle$ in eq 16 were varied until the observed g values were reproduced with physically reasonable parameters. This procedure provides the rotation matrix which gives the molecular **g** tensor coordinate system relative to the Cu_A coordinate system. This rotation is given in Table VI in terms of ϕ, the angle between $g_\parallel$ and $g_z{}^{Cu_A}$, and γ, the angle between $g_\parallel$ and $g_z{}^{Cu_B}$. The trend to reduced $g_\parallel$ value down the half-met series is a direct consequence of the noncolinearity of the coordinate systems on Cu_A and Cu_B. The net dimer **g** tensor is essentially a delocalization weighted vector sum of the $\mathbf{g}^{Cu_A}$ and $\mathbf{g}^{Cu_B}$ tensors: $\mathbf{g}^{dimer} = (1 - \alpha^2)\mathbf{g}^{Cu_A} + \alpha^2\mathbf{g}^{Cu_B}$. As delocalization increases the contribution of $\mathbf{g}^{Cu_B}$ increases and that of $\mathbf{g}^{Cu_A}$ decreases. If the principal axes of the single site **g** tensors are not colinear, then the tensor sum yields a decreased magnitude of $g_\parallel$ for the dimer relative to a completely localized system. Thus, delocalization within a mixed-valent dimer where the orientations of the single site g values are not coincident results in a systematic decrease in the dimer $g_\parallel$.

Half-Met-Halides: Hyperfine Couplings. The hyperfine coupling constants down the half-met-halide series also exhibit an interesting trend with $A_\parallel{}^{Cu_A}$ remaining relatively constant, but $A_\parallel{}^{Cu_B}$ increasing down the series. A complication in the hyperfine analysis of the half-met-halides is that the principal axes of the single site **A** tensors and the dimer **g** tensor are not parallel. The

Table VI. Hyperfine Analysis for Half-Met-L

L	ϕ (deg)[a]	γ (deg)[b]	$A_z^{Cu_A}$ ($\times 10^{-4}$ cm^{-1})	$A_F^{Cu_A}$ ($\times 10^{-4}$ cm^{-1})	$A_z^{Cu_B}$ ($\times 10^{-4}$ cm^{-1})	$(A_F^{Cu_B})'$ [c] ($\times 10^{-4}$ cm^{-1})	A_F^{tot} [d] ($\times 10^{-4}$ cm^{-1})	α^2_{EPR}
NO$_2^-$	(0)		−132	−100	<15	>−6	−106	<0.06
Cl$^-$	1	36	−96	−55	<15	>−6	−61	<0.09
Br$^-$	1.5	32	−92	−49	−44	−21	−70	0.30
I$^-$	4	21	−109	−54	−99	−56	−110	0.30 < α^2 < 0.50

[a] Angle between $A_z^{Cu_A}$ and $g_{\parallel}$. [b] Angle between $A_z^{Cu_B}$ and $g_{\parallel}$. [c] Scaled value obtained as described in the text. [d] $A_F^{tot} = A_F^{Cu_A} + (A_F^{Cu_B})'$.

experimentally observed $A_{\parallel}^i$ is the projection of the $\mathbf{A}^i$ tensor onto the molecular $\mathbf{g}$ tensor: $(A_{\parallel}^i)^2 = \cos^2 \phi \, (A_z^i)^2 + \sin^2 \phi \, (A_{xy}^i)^2$ where ϕ is the angle between the direction of $g_{\parallel}$ and $A_z^{(i)}$. For most monomeric copper systems the direction of A_z is close to that of g_z. It is therefore expected that $A_z^{Cu_A}$ is oriented parallel to $g_z^{Cu_A}$ and $A_z^{Cu_B}$ is likewise oriented parallel to $g_z^{Cu_B}$ and the transformations relating the single site $\mathbf{g}$ tensors to the dimer $\mathbf{g}$ tensor also relate the single site hyperfine parameters to the dimer $\mathbf{g}$ tensor. The intrinsic hyperfine constants can thus be calculated from the simulated values and the rotational angles ϕ and γ and are given in Table VI. The noncoincidence of $\mathbf{g}$ and $\mathbf{A}$ becomes important as γ increases and as the magnitude of the hyperfine coupling to Cu$_B$ increases. Although half-met-Cl$^-$ exhibits the largest noncoincidence of $g_{\parallel}$ and $A_z^{Cu_B}$, the value of $A_z^{Cu_B}$ is small and the general appearance of the spectrum is not significantly affected. In contrast, the half-met-I$^-$ site has a somewhat smaller value of γ, but the much larger $A_z^{Cu_B}$ due to increased delocalization (vide infra) causes the effects of noncoincidence to be most pronounced in this case. The simulations do not account for these effects and thus cannot accurately reproduce the observed EPR features. This accounts for the quality of the half-met-I$^-$ simulations in Figure 5 and limits the accuracy of the simulation parameters given in Table II for this derivative.

A direct independent measure of the electron density at each copper atom can be determined from the parameters governing the hyperfine coupling. On the simplest level, one would expect that $\alpha^2_{EPR} = A_z^{Cu_B}/(A_z^{Cu_A} + A_z^{Cu_B})$. However, it is well established that the magnitudes of hyperfine couplings for monomeric Cu(II) complexes are a sensitive function of geometry.[33] Since the geometry of Cu$_B$ is different from Cu$_A$ and varies over the series, this must be taken into account in a quantitative evaluation of α^2_{EPR}.

For the half-met-halides there is no $|z^2\rangle$ character in the ground state, and for each copper in the site eq 20 reduces in axial symmetry[25] to eq 21.

$$A_z^i = P_d[\kappa^i - (4/7)(\xi^i)^2 + (3/7)\Delta g_{\perp}^i + \Delta g_{\parallel}^i]$$
$$= A_F^i + A_S^i + A_L^i \qquad (21)$$

For each copper in the active site a value of $A_F^i = A_z^i - A_S^i - A_L^i$ can be calculated using eq 20b to estimate the g-value shifts. However, $(\xi^i)^2$ is undetermined and A_F can only be computed as a function of $(\xi^i)^2$. Further, the A_F^i values for Cu$_A$ and Cu$_B$ cannot be compared directly since A_F^i is itself a function of geometry due to variation in the indirect spin polarization.[33b] The Fermi contact term for D_{4h} CuCl$_4^{2-}$ ($\beta = 90°$, $\xi^2 = 0.61$) is -123×10^{-4} cm^{-1} and for D_{2d} CuCl$_4^{2-}$ ($\beta = 62°$, $\xi^2 = 0.67$) is -77×10^{-4} cm^{-1}. Thus for a fixed value of $(\xi^{Cu_B})^2$, $A_F^{Cu_B}$ values can be scaled to those expected for the same electron density in a D_{4h} environment $(A_F^{Cu_B})' = KA_F^{Cu_B}$, assuming the relation between A_F and β is linear in the range $\beta = 60-90°$.[36] Delocalization can then be directly computed by eq 22.

$$\alpha^2_{EPR} = (A_F^{Cu_B})'/(A_F^{Cu_A} + (A_F^{Cu_B})') \qquad (22)$$

The relationships between the $(\xi^i)^2$, α^2, a^2, and b^2 (defined in eq 17) are given in eq 23.

$$(\xi^{Cu_A})^2 = a^2 = \alpha^2(\xi_{tot})^2 \qquad (23a)$$
$$(\xi^{Cu_B})^2 = b^2 = (1 - \alpha^2)(\xi_{tot})^2 \qquad (23b)$$
$$(\xi_{tot})^2 = (\xi^{Cu_A})^2 + (\xi^{Cu_B})^2 \qquad (23c)$$

(36) Based on the values of A_F and β for D_{4h} and D_{2d} CuCl$_4^{2-}$, $K = 3.42 - 0.027\beta$.

For a fixed value of $(\xi_{tot})^2$, $(\xi^{Cu_A})^2$ and $(\xi^{Cu_B})^2$ can be initially estimated from $(\xi^{Cu_A})^2 = A_z^{Cu_A}/(A_z^{Cu_A} + A_z^{Cu_B})$ and eq 23c. Based on these estimates, A_F^i values can be calculated from eq 20b and 21 which in turn determine α^2 from eq 22. Equation 23 then provides new values of $(\xi^{Cu_A})^2$ ($=a^2$) and $(\xi^{Cu_B})^2$ ($=b^2$). These relationships (eq 21-23) suggest an iterative approach in which a value of $(\xi_{tot})^2$ is chosen and a^2, b^2, and α^2 are allowed to converge to a set of parameters consistent with eq 21-23. For the half-met-halides with $(\xi_{tot})^2 = 0.70-0.80$ this procedure gives[37] the $A_F^{Cu_A}$ and $(A_F^{Cu_B})'$ parameters in Table VI.

The values of α^2_{EPR} computed from eq 22 are presented in Table VI. The estimated α^2_{EPR} is in each case larger than α^2_{opt} in Table IV by at least a factor of 10. This disparity between α^2_{opt} and α^2_{EPR} provides a quantitative estimate of the divergence of the formalism of eq 13 as delocalization approaches intermediate values (vide infra). Further, the decrease of A_F^{tot}, and thus total metal character, for half-met-Cl$^-$ and -Br$^-$ relative to NO$_2^-$ indicates the increase in covalency for these sites relative to the fully localized NO$_2^-$ derivative. The inability to precisely define the half-met-I$^-$ parameters due to noncoincidence of the $\mathbf{g}$ and $\mathbf{A}$ tensors results in greater uncertainty in these parameters. This difficulty is clearly manifested in the unrealistically large value of A_F^{tot}. However, based on the observation of larger hyperfine coupling constants for Cu$_B$ in this case, α^2_{EPR} for half-met-I$^-$ must have a value between that of half-met-Br$^-$ and the completely delocalized value of $\alpha^2 = 0.5$.

LEFE Analysis. The LEFE data in Figure 6 can be used as an important complementary probe of the mixed-valent character of the ground state of the half-met site. The experimental LEFE shift parameter σ is related to the shift in the g value upon application of an electric field E by eq 24 where $K \approx 1$.

$$\sigma = K|\delta g/g|_{ave}E^{-1} \qquad (24)$$

A *linear* electric field induced shift can only occur when the ground state consists of a mixture of odd and even parity wave functions, and this, in turn, can only occur when the site is noncentrosymmetric. The magnitude of the shift depends on the extent of the odd-even mixing and on the deviation from centrosymmetry of the site.

The electric field induced shift in the resonance frequency or g value is described[38] by a third-rank tensor containing 18 g^2-shift coefficients (Voigt notation) defined in eq 25.

$$B_{ij} = \partial(g_j^2)/\partial E_i \qquad (i = 1, 2, 3 \, (=x, y, z) \text{ and } j = 1-6) \qquad (25)$$

For $j = 1, 2, 3$ the nine B_{ij} terms are due to electric field induced shifts of the principal g^2 values; the remaining nine terms ($j =$

(37) This procedure does not converge for half-met-Cl$^-$ due to the indeterminacy of $A_z^{Cu_B}$ but oscillates through a wide range of values. As an alternative approach A_z^i for each copper was calculated explicitly from eq 21 as a function of $(\xi^i)^2$ and $A_{\perp}^i$ was calculated from[25]

$$A_{\perp}^i = P_d[\kappa^i + (2/7)(\xi^i)^2 + (11/4)\Delta g_{\perp}^i]$$

For this calculation A_F^i was taken as the A_F value for CuCl$_4^{2-}$ in the appropriate geometry (D_{4h} for Cu$_A$ and D_{2d} ($\beta = 62°$) for Cu$_B$) scaled by the electron density at the nucleus relative to that for CuCl$_4^{2-}$. For example, the $A_F^{Cu_A}$ value was taken as $((\xi^{Cu_A})^2/0.61)(-123 \times 10^{-4}$ cm$^{-1})$ where 0.61 is the unpaired spin density at copper for D_{4h} CuCl$_4^{2-}$. From the calculated A_z^i and $A_{\perp}^i$, only a narrow range of $(\xi^i)^2$ and thus A_F^i were consistent with the experimental A_z^i values and the lack of resolution of any $A_{\perp}^i$ features ($|A_{\perp}^i| < 15 \times 10^{-4}$ cm^{-1}) and these are reported in Table II.

(38) Mims, W. B. *The Linear Electric Field Effect in Paramagnetic Resonance*; Clarendon: Oxford, 1976.

6120 *J. Am. Chem. Soc., Vol. 111, No. 16, 1989*

Westmoreland et al.

Table VII. Nonzero g^2-Shift Parameters for Selected Symmetries

	principal g^2 shifts			off-diagonal g^2 shifts	
D_{2d}				B_{14}	B_{36}
C_{4v}	B_{31}		B_{33}	B_{15}	
C_{2v}	B_{31}	B_{32}	B_{33}	B_{15}	B_{24}
C_s	B_{11}	B_{12}	B_{13}	B_{15}	B_{24}
	B_{31}	B_{32}	B_{33}	B_{26}	B_{35}

4, 5, 6) arise from electric field induced off-diagonal g^2 elements and can be thought of as a small tilting of the $\mathbf{g}^2$ tensor by the electric field. As summarized in Table VII, the symmetry of the paramagnetic site dictates[39] which B_{ij} terms will be nonzero, and different odd parity distortions from a centrosymmetric geometry will lead to quantitatively different LEFE spectra. For a particular symmetry, the B_{ij} terms which contribute to an experimentally measured shift will depend upon the relative orientation of the electric and magnetic fields and upon the molecular orientation (i.e., g value setting) across the EPR spectrum. While several terms may contribute to the observed shift at magnetic field settings across the EPR spectrum, at the extreme g values the situation is simplified. In particular, the g shift parameters at $g_\parallel$ ($g_z = g_3$) for E∥H and for E⊥H, in axial symmetry, are given in eq 26 and 27, respectively.

$$\sigma_{\parallel,3} = B_{33}/2g_z^2 \tag{26}$$

$$\sigma_{\perp,3} = (B_{13}^2 + B_{23}^2)^{1/2}/(2.90g_z^2) \tag{27}$$

The B_{ij} contributions to the entire LEFE spectrum have been examined[40] in simulations of E∥H and E⊥H shifts for two common noncentrosymmetric Cu(II) geometries, D_{2d} and C_{4v}. The major spectral difference found between these two symmetries lies at $g_\parallel$. The B_{13}, B_{23}, and B_{33} terms are all zero in D_{2d} symmetry (Table VII) and there is no shift at $g_\parallel$ for either E∥H or E⊥H. However, in C_{4v} symmetry B_{33} is allowed (Table VII) and an E∥H shift at $g_\parallel$ is observed. To examine individual contributions of the B_{ij} terms to the entire LEFE spectrum, the magnetic field (g value) dependence of E∥H and E⊥H shifts for each of the 18 B_{ij} terms has been calculated[41] for a rhombic site ($g_1 = 1.7$, $g_2 = 2.2$ $g_3 = 2.8$). These normalized simulations (Figures 5 and 6 of ref 41) provide a basis for analyzing individual B_{ij} contributions to an experimental LEFE spectrum.

A perturbation spin Hamiltonian used in calculating the g^2-shift parameters, B_{ij}, which includes spin-orbit coupling, Zeeman, and electric dipole terms is given in eq 28 where the hyperfine interaction has been neglected.

$$\mathcal{H}' = \lambda L \cdot S + \beta H(L + 2.00S) + e\mathbf{E} \cdot \mathbf{r} \tag{28}$$

In analyzing the LEFE in the mononuclear blue copper protein azurin, Gerstman and Brill[42] recently derived a general third-order perturbation expression for the ligand field origin of the closely related parameter C_{ij} where

$$B_{ij} = 2g_j C_{ij} \tag{29}$$

At the principal g values the C_{ij} are given by eq 30 where $\langle G|$ is the ground state, and $\langle M|$ and $\langle Q|$ are excited states.

$$
\begin{aligned}
C_{ij} = 4e\{ & \sum_{M \neq G} \sum_{Q \neq G} (\langle G|r_i|M\rangle\langle M|L_j|Q\rangle\langle Q|\lambda L_j|G\rangle \\
& + \langle G|r_i|M\rangle\langle M|\lambda L_j|Q\rangle\langle Q|L_j|G\rangle \\
& + \langle G|L_j|M\rangle\langle M|r_i|Q\rangle\langle Q|\lambda L_j|G\rangle)/(E_M - E_G)(E_Q - E_G) \\
& - \sum_{M \neq G} (\langle G|r_i|G\rangle\langle G|L_j|M\rangle\langle M|\lambda L_j|G\rangle)/(E_M - E_G)^2\}
\end{aligned}
\tag{30}
$$

The four terms in eq 30 contain matrix elements consisting of orbital angular momentum coupling of the ground and excited states and between excited states, as well as matrix elements for

(39) Smith, C. S. In *Solid State Physics*; Seitz, F., Turnbull, D., Eds.; Academic Press: New York, 1958; Vol. 6, p 175.

(40) Mims, W. B.; Peterson, G. E.; Kurkjian, C. R. *Phys. Chem. Glasses* **1978**, *19*, 14.

(41) Mims, W. B.; Peisach, J. *J. Chem. Phys.* **1976**, *64*, 1074.

(42) Gerstman, B. S.; Brill, A. S. *Phys. Rev. A* **1988**, *37*, 2151.

Table VIII. Experimental LEFE Parameters for Half-Met-L Hemocyanin

	L				
	NO_2^-	OAc⁻	Cl⁻	Br⁻	I⁻
$g_\parallel$	2.302	2.318	2.347	2.312	2.261
$\sigma_{\parallel,3}$ ($\times10^{-9}$ V⁻¹ cm)	0.510	0.385	0.403	0.367	0.382
C_{33} ($\times10^{-5}$ Å/cm⁻¹)	0.874	0.664	0.704	0.631	0.643
$\sigma_{\perp,3}$ ($\times10^{-9}$ V⁻¹ cm⁻¹)	0.352	0.280	0.356	0.318	0.294
$C_{\perp3}$ ($\times10^{-5}$ Å/cm⁻¹)	0.619	0.495	0.638	0.561	0.507
$\sigma_{\parallel,max}$ ($\times10^{-9}$ V⁻¹ cm)	0.550	0.445	0.532	0.485	0.395
L → Cu(II) charge transfer					
E_{max}, cm⁻¹ (ε, M⁻¹ cm⁻¹)	>25000[a]	>25000[a]	24150 (~20)	23560 (68)	19230 (200)

[a]Not observed.

electric dipole coupling of the ground and excited states, between excited states, and within the ground state. These latter matrix elements require the mixing of odd parity components into the ground state for C_{ij} to be nonzero.

Table VIII lists the experimental LEFE parameters at $g_\parallel$, $\sigma_{\parallel,3}$ and $\sigma_{\perp,3}$, for the LEFE spectra in Figure 6 and for half-met-OAc⁻. These values have also been converted into C_{33} and $C_{\perp3}$ ($=[(C_{13}^2 + C_{23}^2)/2]^{1/2}$) values in units of Å/cm⁻¹ using eq 27, 28, and 30, and a Lorentz factor ($R = 5/3$) to account for the local electric field.[42] Table VIII also indicates the maximum experimental E∥H shift, $\sigma_{\parallel,max}$ for any magnetic field setting, and the energy and intensity of the exogenous ligand-to-Cu(II) charge-transfer transition for each half-met derivative.

The ligand field transitions of half-met-NO_2^- and the other half-met-L derivatives indicate that the Cu(II) ion has an approximately tetragonal coordination geometry. The observed nonzero electric field induced shift in the g values requires a noncentrosymmetric Cu(II) site, and specifically the larger shift for E∥H at $g_\parallel$ indicates that C_{4v} is an appropriate initial effective symmetry. However, the appreciable shift for E⊥H at $g_\parallel$ requires a lower site symmetry; Table VII indicates that C_s symmetry is necessary since it results in a nonzero B_{13} term as required by the E⊥H shift at $g_\parallel$, eq 27. In Brill's analysis of the azurin LEFE data[42] it was shown, using calculations based on a hybrid atomic orbital model (HAOM), that ground-state mixing of $4p_z$ and 4s resulted in nonzero C_{33} values and that mixing of $4p_x$ and/or $4p_y$ resulted in a nonzero $C_{\perp3}$. Further, one calculation which used a ground state with 69.3% $3d_{xy}$, 26.6% $4p_z$, 2.2% 4s, 1.0% $4p_x$, and 1.0% $4p_y$ resulted in shift values ($C_{33} = -0.94 \times 10^{-5}$ Å/cm⁻¹ and $C_{\perp3} = 0.65 \times 10^{-5}$ Å/cm⁻¹) quite similar to those of half-met-NO_2^- (Table VIII). While the HAOM includes only Cu atomic orbital mixing, the non-d-orbital ground-state components can be correlated with ligand covalency and reflect the mixing of charge-transfer states of similar symmetry in a molecular orbital analysis. Thus the experimental LEFE data for half-met-NO_2^- and quantitative comparison to calculations of C_{33} and $C_{\perp3}$ indicate a Cu(II) site of C_s symmetry with $4p_z$, 4s, and $4p_x$, (mirror plane defined as yz) or molecular orbital components of the same symmetry mixing into the ground state.

In comparison to half-met-NO_2^-, half-met-OAc⁻ and -Cl⁻ show a decrease in $\sigma_{\parallel,3}$ and thus a quantitatively smaller B_{33} term. Based on the calculations indicated above,[42] this corresponds to a decrease in the 4s and/or $4p_z$ components of the ground state. The rhombic splitting of g_x and g_y in half-met-NO_2^- is also lost in the axial OAc⁻ and Cl⁻ derivatives. The degree of rhombic splitting directly correlates with the amount of $3d_{z^2}$ character in the ground state; however, for square-planar $CuCl_4^{2-}$ it has been shown[33] that d_{z^2} mixing also carried with it 4s character. Thus a reasonable origin for the decreased E∥H shift at $g_\parallel$ in half-met-OAc⁻ and -Cl⁻ is a reduced mixing of 4s into the $d_{x^2-y^2}$ ground states which is also reflected in the loss of rhombic splitting in their EPR spectra.

Also in comparison to half-met-NO_2^- the E⊥H shift at $g_\parallel$ is observed to decrease in half-met-OAc⁻ while for Cl⁻ it increases somewhat. As described above, the magnitude of $\sigma_{\perp,3}$ correlates with $4p_x$ mixing into the ground state, and this odd parity component can be associated with an equatorial ligand-to-Cu(II) CT transition. Such a low-energy excited state is found (Table VIII)

for Cl⁻ but not OAc⁻ or NO_2^-. The increased $E \perp H$ shift at $g_\parallel$ of half-met-Cl⁻ relative to -OAc⁻ therefore appears to reflect a ground-state odd-parity contribution of the Cl⁻ → Cu(II) CT transition.

In Figure 6, half-met-Cl⁻ and -OAc⁻ both show a maximum in their $E \parallel H$ shifts at fields away from $g_\parallel$. In a crystal field analysis of the individual B_{ij} contributions to the LEFE spectrum, it was found[41] that the amplitude factor of the spherical harmonic associated with B_{13} is the same amplitude factor that determines the magnitude of one other g^2-shift term, B_{35}, which is nonzero in C_s symmetry. Based on the calculations[41] of the 18 B_{ij} terms this component has a larger shift for $E \parallel H$ than $E \perp H$ between $g_\parallel$ and $g_\perp$. The large maximum away from $g_\parallel$ in the $E \parallel H$ shifts thus appears to reflect a contribution of B_{35} to the LEFE spectrum. Further, as B_{13} quantitatively increases, the B_{35} contribution to the LEFE spectrum should also increase. This is observed in comparing half-met-OAc⁻ and -Cl⁻ where the increased magnitude of the Cl⁻ $E \parallel H$ maximum, quantified by the $\sigma_{\parallel,max}$ value, parallels the increased magnitude of $\sigma_{\perp,3}$ (Table VIII).

Although qualitative differences are small between the LEFE data of the half-met-halides, quantitatively a decrease is observed (Table VIII) both in $\sigma_{\perp,3}$ and in $\sigma_{\parallel,max}$ on going down the halide series. Also changing in this series is a shift to lower energy and an increase in intensity of the equatorial L → Cu(II) CT transition (Table VIII). This should introduce a progressively larger odd-parity term of the same symmetry as $4p_x$ into the ground state, increase the B_{13} contribution, and thus increase $\sigma_{\perp,3}$ in the LEFE spectrum. However, this is just the opposite of what is experimentally observed. Likewise, B_{35} is also expected to increase, leading to an increased magnitude for the maximum in the $E \parallel H$ spectrum. This is also not observed; in fact, the decrease in the $E \parallel H$ maximum ($\sigma_{\parallel,max}$ in Table VIII) is the most noticeable change in the LEFE spectra of the half-met halides.

Thus, the quantitative decrease in the $E \perp H$ shift at $g_\parallel$ (B_{13}) and the maximum in the $E \parallel H$ shift in the middle of the EPR spectrum (B_{35}) does not correlate with the low-energy L → Cu(II) charge-transfer component of the ground state of the half-met halides. Finally, we note that down the half-met series there is also an increase in the delocalization of the ground state over both coppers of the mixed-valent half-met site, and the LEFE data appear to indicate that this increased delocalization results in a decrease in the odd-parity character of the mixed-valent ground state.

Discussion

Mixed-Valent Properties. Spectroscopic analysis of the half-met hemocyanins has provided significant insight into the electronic properties of binuclear mixed-valent complexes. Delocalization in the half-met ground state has been estimated by two independent means: (1) α^2_{opt} from a Hush analysis of the IT band intensity (Table IV) and (2) α^2_{EPR} from the relative Fermi contact terms for each copper as calculated from the hyperfine coupling parameters (Table VI). The values from the hyperfine analysis are at least an order of magnitude larger than those calculated from eq 13a. The Hush equations are appropriate for a nearly localized limit and are expected to underestimate delocalization as the system becomes significantly delocalized. This divergence appears to arise[43] from the approximations associated with the evaluation of the transition dipole matrix element, ⟨IT|er|G⟩ where |G⟩ and |IT⟩ are given in eq 1 and 2. Explicit evaluation of the matrix element gives eq 31.[44]

$$\langle IT|er|G \rangle = \alpha(1 - \alpha^2)^{1/2}e(r_A - r_B) + (1 - \alpha^2)eS(r_{AB} - r_B) \tag{31}$$

In eq 31 $(r_A - r_B)$ is the transition dipole associated with the transfer of an electron from Cu_B to Cu_A. S is the overlap integral between the localized wave functions $|\psi[Cu_A(II)Cu_B(I)]\rangle$ and $|\psi[Cu_A(I)Cu_B(II)]\rangle$, and $(r_{AB} - r_B)$ represents the dipole moment associated with the transfer of an electron from the $Cu_A Cu_B$

overlap region to Cu_A. Most treatments of CT intensity, including the Hush equations, retain only the first term which is dominant for small S. This is usually written as ⟨IT|er|G⟩ = αeR where the ground- and excited-state wave functions used are not normalized (and $\alpha^2 \ll 0.5$) and R is the Cu_A–Cu_B distance. As delocalization increases, the values of both α^2 and S increase, and the second term can make a significant contribution to the IT intensity. The limitation of the IT intensity analysis thus appears to derive from the reasonable overlap between the Cu_A and Cu_B sites in the half-met hemocyanin ground state. In contrast, the hyperfine analysis does not require small values of delocalization and, in fact, is more accurate at moderate values of α^2 for which the hyperfine couplings of both coppers can be resolved. The delocalization parameters in Tables IV and VI represent experimental confirmation of the limitation of the IT intensity formalism for estimating delocalization at moderate values of α^2.

A new feature arising from delocalization in the dimer is that there is a severe noncoincidence of the directions of the principal axes of the dimer **g** tensor and the Cu hyperfine tensors. This noncoincidence arises from delocalization of the unpaired spin over metal sites with very different local coordinate orientations. There are two major effects on the EPR spectra in such systems.[45] The maximum hyperfine splitting occurs at a g value which does not correspond to one of the principal g values. Thus, the observed intensity across the EPR spectrum is a complicated function of both the field direction and the angle between **g** and A^l. Additionally, the hyperfine features at the principal g values are not necessarily evenly spaced since the extrema for each hyperfine resonance may be different. The phenomenological effects are evident in the EPR spectra of half-met-I⁻ in Figure 5. Although the Q-band spectrum can be successfully simulated because of the lack of resolution of the hyperfine structure, the S-band and X-band simulations do not reproduce the observed hyperfine intensity patterns. The net effect of **g** and **A** tensor noncoincidence is to cause significant anomalous intensity between $g_\parallel$ and $g_\perp$. Extending the analysis to an even more delocalized site, it is possible that the unusual low-temperature (<20 K) X-band spectrum of half-met-N_3^- (Figure 8 of ref 1a) may arise primarily from a severe noncoincidence of the **g** and **A** tensors.

LEFE measurements have provided an important new probe of delocalization in mixed-valent systems. The magnitude of the LEFE in general correlates with the odd-parity component in the ligand field potential of the unpaired electron. As obtained in the analysis, the LEFE spectra do not show the expected correlation with the LMCT transition energy and intensity, and, in fact, the decrease in the magnitude of the LEFE down the half-met series indicates that increased delocalization decreases the odd-parity contribution to the ground state. This can be understood by evaluating the electronic part of the Stark operator, er, over the ground-state wave function given in eq 1.

$$\langle G|er|G \rangle =$$
$$(1 - \alpha^2)\langle \psi[Cu_A(II)Cu_B(I)]|er_A|\psi[Cu_A(II)Cu_B(I)]\rangle +$$
$$\alpha^2\langle \psi[Cu_A(I)Cu_B(II)]|er_B|\psi[Cu_A(I)Cu_B(II)]\rangle + (1 - 2\alpha^2)eR_{AB} \tag{32}$$

In eq 32 r_A and r_B are defined with respect to Cu_A and Cu_B coordinates and R_{AB} is the vector from Cu_B to Cu_A. The last term represents the static dipole associated with the ground state. This contribution causes no additional shift in the g values since it changes the energy of both components of the ground-state spin manifold by an equal amount in the same direction. Note that, as might be expected, this molecular dipole moment decreases as delocalization increases and becomes zero in a Class III complex with $\alpha^2 = 0.5$. The first two terms on the right in eq 33 represent the local odd-parity contributions to the ligand fields at the Cu_A and Cu_B sites, respectively. Thus the LEFE is the sum of the LEFE signals of the individual ions, which are expected to correlate with the mixing of the L → Cu CT transitions into the ground state, which increases from Cl⁻ to I⁻. These terms are, however,

(43) Wong, K. Y.; Schatz, P. N. *Prog. Inorg. Chem.* **1981**, *28*, 369.
(44) Mulliken, R. S. *J. Am. Chem. Soc.* **1952**, *74*, 811.

(45) Pilbrow, J. R.; Lowery, M. R. *Rep. Prog. Phys.* **1980**, *43*, 433.
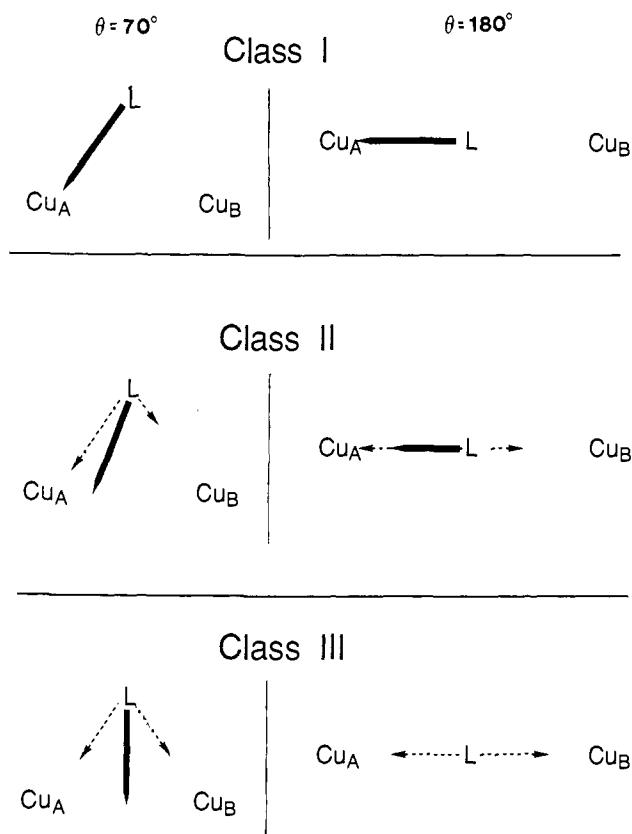
Figure 15. Vector addition of local CT vectors, r_A and r_B (dashed arrows), to give the net CT vector, r_{tot} (solid arrow), as a function of delocalization for $\theta = 70°$ (left) and $\theta = 180°$ (right).

vector quantities. Expressing the net LEFE contribution as proportional to r_{tot} and the individual contributions as r_A and r_B, the predicted magnitude of the LEFE decreases with delocalization as illustrated in Figure 15 with $\theta = 70°$, which is appropriate for the half-met hemocyanin site (vide supra). r_A and r_B tend to partially cancel for a fixed magnitude of $|r_A| + |r_B|$. Thus, the *decrease* of the magnitude of the LEFE with increasing IT band intensity distinguishes the effects of delocalization from simple LMCT mixing effects such as found for monomeric Cu(II). It is interesting to extend this analysis to a linearly bridged system ($\theta = 180°$) as shown in Figure 15. For the completely delocalized Class III case, the site now has inversion symmetry in the dimer, and the local odd-parity contributions on each copper cancel exactly resulting in the absence of an LEFE on the spin–echo EPR spectrum.

The Half-Met Active Site. The half-met hemocyanin site represents a one-electron intermediate between the fully oxidized and fully reduced forms of a two-electron site. Previous studies on tyrosinase,[46] which contains a very similar binuclear site, have shown that the met-aquo tyrosinase site is reduced by two electrons at the same potential. The half-met-aquo derivatives of both tyrosinase and hemocyanin may thus be expected to be unstable with respect to disproportionation. In the absence of a small molecule redox mediator, however, there is no favorable mechanism for electron transfer. Thus half-met-aquo tyrosinase and hemocyanin are kinetically trapped but thermodynamically unstable intermediates. The thermodynamic results in Table I indicate that binding of N_3^- to the half-met-aquo hemocyanin site stabilizes this derivative with respect to disproportionation by four orders of magnitude. The values of $\Delta G°_{deloc}$ in Table IV further indicate that the thermodynamic effects of delocalization are probably negligible for all half-met hemocyanins. Thus, the stabilization relative to half-met-aquo must relate to the geometry of the half-met-L site relative to the corresponding met-L or

deoxy-L sites. The thermodynamic parameters in Table I indicate that this stabilization is driven by a highly favorable entropy of binding.

Previously reported synthetic binuclear mixed-valent copper complexes fall into one of two categories.[47] Mostly, they are strongly localized Class I systems with clearly tetragonal Cu(II) sites and distorted tetrahedral Cu(I) sites. In a few cases,[47b] the geometric constraints imposed by the chelate ligand force the two coppers to have approximately the same geometry, and these complexes exhibit Class III delocalized properties. The half-met hemocyanins are thus far unique among mixed-valent copper dimers in that they are capable of sustaining an intermediate Class II site and the substitution chemistry that has been developed[6] allows for variation of the exogenous ligand and the extent of delocalization in a straightforward and systematic fashion. The geometry of the half-met-L site has been established based on the spectroscopic properties of the site as presented in the Analysis section. From the optical absorption, CD, and LT-MCD spectra the $Cu_A(II)$ geometry is tetragonal while a ligand field analysis of the IT band energy has determined that $Cu_B(I)$ has a distorted tetrahedral geometry. From previous studies[6] there is considerable evidence that the exogenous ligand, L, bridges the two coppers and that, with the exception of the half-met-xs-L derivatives (see ref 6 for a detailed discussion of this chemistry), there also appears to be an endogenous bridging ligand present. Based on these results, the spectroscopically effective active site of half-met-L hemocyanin has been determined and is given in Figure 14.

An interesting feature of the half-met-L site is that the geometry of $Cu_B(I)$ is strongly correlated with the extent of delocalization. Half-met-Cl⁻, in which Cu_B has the least Cu(II) character, exhibits the least distortion of Cu_B from tetrahedral geometry ($\beta_{eff} = 62°$). In contrast, the nearly delocalized half-met-I⁻ shows the largest distortion toward a tetragonal geometry ($\beta_{eff} = 72°$). These results are consistent with the calculations of Sherwood and Hoffmann[48] which show that for a hypothetical localized mixed-valent dimer, $[Cu_2Cl_6]^{3-}$, the total energy of the system is minimized if the Cu(I) has local distorted T_d symmetry and the Cu(II) has a tetragonal geometry. Further, as delocalization is increased the energy is minimized toward geometries which are distorted toward more equivalent sites.

Since there are both exogenous and endogenous bridging ligands, there are two possible pathways for the electronic coupling which leads to delocalization. In general, delocalization is through a superexchange pathway which requires nonorthogonal orbitals. The key parameter is the MLM angle, which must be different from 90° for efficient σ orbital overlap with the half-occupied $|x^2-y^2\rangle$ orbital on Cu_A. As shown in Table V, for each member of the halide series the CuLCu angle, θ, is sufficiently different from 90° such that efficient coupling via exogenous ligand orbital overlap is possible. However, the endogenous bridge (OR⁻) may provide an effective pathway for delocalization and, in fact, is responsible for antiferromagnetically coupling the two Cu(II) centers in the met derivatives.[49] From the geometry calculation, the Cu(OR⁻)Cu angle, ρ, is seen to increase down the halide series and could be the basis of better overlap through OR⁻ and hence increase delocalization. However, similar calculations for half-met-NO_2^- and half-met-OAc⁻ are also presented in Table V for a number of possible bridging geometries. In each case ρ is sufficiently different from 90° that these derivatives would be expected to be delocalized if OR⁻ were the pathway for delocalization. However, from Figure 4 (half-met-NO_2^-) and Figure 1A of ref 6 (half-met-OAc⁻), both of these derivatives are localized and OR⁻ does not play a dominant role in delocalization. Thus the mixed-valent properties of the half-met-L series are the result of electronic coupling of the two coppers through L and require that exogenous ligands bridge between the two copper ions in the

(46) Makino, N.; McMahill, P.; Mason, H. S. *J. Biol. Chem.* **1974,** *249,* 6062.

(47) (a) Dunaj-Jurco, M.; Ondrejovic, G.; Melnik, M.; Garaj, J. *Coord. Chem. Rev.* **1988,** *83,* 1. (b) Gagne, R. R.; Koval, C. A.; Smith, T. J.; Cimolino, M. C. *J. Am. Chem. Soc.* **1979,** *101,* 4571.

(48) Sherwood, P.; Hoffmann, R. *Inorg. Chem.* **1989,** *28,* 509.

(49) Wilcox, D. E.; Long, J. R.; Solomon, E. I. *J. Am. Chem. Soc.* **1984,** *106,* 2186.

site. The decrease in θ down the half-met-halide series may contribute somewhat to the increase in delocalization from Cl⁻ to Br⁻ to I⁻; however, increasing metal–ligand covalency probably dominates. Thus for a superexchange pathway delocalization should correlate with LMCT mixing. α can be expressed in terms of charge-transfer mixing through second-order perturbation theory as given in eq 33.[50]

$$\alpha = \frac{\langle G|H|N(LMCT)\rangle\langle N(LMCT)|H|IT\rangle}{(E_{IT} - E_G)(E_N - E_G)} \quad (33)$$

From eq 33, α and thus delocalization increases with increasing LMCT state mixing into both the ground and IT states and with decreasing LMCT energy. This is in qualitative agreement with the LMCT energies and intensities for the half-met series as given at the bottom of Table VIII.

These results provide insight into the active site of the multi-copper oxidase laccase, which couples four one-electron substrate oxidations to the four-electron reduction of O_2 to H_2O. The native enzyme contains a blue copper site (Type 1), a "normal" copper site (Type 2), and a coupled binuclear copper site (Type 3). A derivative has been prepared in which the Type 2 copper has been removed (the Type 2 depleted, T2D, derivative) and the Type 3 site has been oxidized to the half-met form.[8] This half-met T2D

site exhibits properties very different from those of the half-met hemocyanins (and tyrosinases). Exogenous ligands can bind to the site, but *without* the high affinities displayed in hemocyanin. Further, the optical absorption spectra of these derivatives show no IT bands and the EPR spectra exhibit no hyperfine features attributable to delocalization within the binuclear site, even for $L = Br^-$, I^-, or N_3^-. Based on the analysis above, this lack of both mixed-valent features and high affinity ligand binding suggests that exogenous ligands do not bridge the coppers in half-met T2D laccase. Thus, the Type 3 site in laccase is fundamentally different from the coupled binuclear sites in hemocyanin and tyrosinase, and this difference appears to be important in understanding the differences in reactivity between these active sites. For the T2D derivatives of laccase, in contrast to hemocyanin, the half-met site is a thermodynamically stable one-electron reduced site, and the deoxy Type 3 site does not react with dioxygen in the absence of the Type 2 copper.

Supplementary Material Available: Tables S1–S4 containing complete parameters for the EPR simulations in Figure 5 (4 pages). Ordering information is given on any current masthead page.

(50) Mayoh, B.; Day, P. *J. Chem. Soc. Dalton Trans.* **1974**, 846.

Chromatic Properties of Polydiacetylene Films

M. Wenzel and G. H. Atkinson*

Contribution from the Department of Chemistry and Optical Sciences Center, University of Arizona, Tucson, Arizona 85721. Received December 7, 1988

Abstract: The thermochromic and proposed visible photochromic properties of PDA-12,8 are examined by resonance Raman (RR) and Fourier transform infrared (FTIR) spectroscopies. The chromatic properties are derived from the conversion of a blue-colored PDA-12,8 material (produced upon ultraviolet-induced polymerization) to a red-colored material. Experiments are performed under well-controlled thermal conditions which aid in separating the ultraviolet polymerization used to generate the blue-colored polymeric material from its well-known thermochromic process and from photochromism proposed to be induced by visible radiation. For example, irradiation at 532 nm of water-cooled (0.5 °C) samples of the blue-colored material produces no chromatic changes. A chromatic change to the red-colored material is induced by 532-nm radiation, however, when the PDA-12,8 is not cooled. No evidence supporting a visible photochromic change in PDA-12,8 is found, and it is proposed that the previously reported chromatic properties derive from thermal effects. RR and FTIR data are presented which demonstrate that separate structural changes in the polydiacetylene backbone and in the hydrocarbon side chains of PDA-12,8 accompany the chromatic changes. RR results also show that no change occurs in the distribution of electron density along the PDA-12,8 backbone when chromatic effects are induced.

The chromatic properties of organic molecules, long of interest in fundamental studies,[1] have recently become important elements in applications directed toward the optical processing of information.[2] For example, there are numerous suggestions for optical data storage based on chromatic changes in organic films or solids with optical bistability being one process of major interest.[3] When such chromatic changes occur rapidly (i.e., $<10^{-8}$ s), the material becomes a candidate for optical switching applications.

Polydiacetylenes (PDA), a class of organic molecules which is well known for its nonlinear optical properties,[4] have now also

been considered for potential applications in the areas mentioned above. In the cases of PDA having urethane substituents in the side group and of polymerized Langmuir–Blodgett films of PDA formed by long-chain aliphatic substituted diacetylene carbonic acids and their salts, chromatic behavior in solution and in the solid state is well known.[5-7] There also are numerous reports of color changes caused by the addition of a nonsolvent to a poly-diacetylene solution[6] or in conjunction with heat treatment in the case of the solid state.[8] A recent series of publications,[9-12]

(1) Brown, G. H. Ed. *Photochromism (Techniques of Chemistry*, Vol. 3); Wiley-Interscience: New York, 1971.
(2) Wilson, A. E. *Phys. Technol.* **1984**, *15*, 232.
(3) Wintgens, V.; Johnston, L. J.; Scianino, J. G. *J. Am. Chem. Soc.* **1988**, *110*, 511.
(4) Carter, G. M.; Chen, Y. J.; Tripathy, S. K. *Appl. Phys. Lett.* **1983**, *43*, 891.

(5) Chance, R. R.; Patel, G. N.; Witt, J. D. *J. Chem. Phys.* **1979**, *71*, 206.
(6) Patel, G. N.; Chance, R. R.; Witt, J. D. *J. Polym. Sci. Polym. Lett. Ed.* **1978**, *16*, 607.
(7) Tieke, B. *Adv. Polym. Sci.* **1985**, *71*, 79.
(8) Chance, R. R.; Baughman, R. H. Muller, H. Eckhardt, C. J. *J. Chem. Phys.* **1979**, *67*, 3616.
(9) Kanetake, T. Tokura, Y.; Koda, T. *Solid State Commun.* **1985**, *56*, 803.